BRNO UNIVERSITY OF TECHNOLOGY

VYSOKÉ UČENÍ TECHNICKÉ V BRNĚ

CENTRAL EUROPEAN INSTITUTE OF TECHNOLOGY BUT

STŘEDOEVROPSKÝ TECHNOLOGICKÝ INSTITUT VUT

NEW NANODEVICES FOR ELECTRONICS - FABRICATION AND CHARACTERIZATION

NOVÉ NANOPRVKY PRO ELEKTRONIKU – PŘÍPRAVA A CHARAKTERIZACE

DOCTORAL THESIS

TEZE

AUTHOR
AUTOR PRÁCE

Ing. Marian Márik

SUPERVISOR
ŠKOLITEL

doc. Ing. Jaromír Hubálek, Ph.D.

BRNO 2021

ABSTRACT

This work proposes a technique for fabrication of a self-ordered nanostructures for electrical applications. The devices were prepared by anodic oxidation in two lengths and three different heat treatments. The structural characterization using SEM, TEM and EDX technics, respectively, were evaluated from structural and material point of view as well. The unique root structure of the highly self-ordered nanocolumn arrays was evaluated and compared after three different heat treatments: as anodized, vacuum annealed and air annealed, respectively. The possible crystallographic orientation of the columns was not observed, however the nano-crystallites under the root structures were found.

The electrical study about the devices shown resistive switching behavior (RS), diode like behavior and a capacitive coupled diode like behavior as well. The active surface, from RS point of view, for the switching mechanism is at the top of the nanocolumns and the gold top electrode. The Schottky barrier height of the Ti/TiO_2 interface was calculated with two methods, and it was lower than 1,11 eV for all three devices.

KEYWORDS

TiO_2, anodic oxidation, resistive switching, Schottky barrier height, nanocolumn, alumina

ABSTRAKT

Táto práca sa zaoberá technikou výroby samousporiadaných nanoštruktúr pre elektrické aplikácie. Prototypy boli pripravené anodickou oxidáciou v dvoch dĺžkach a tromi rôznymi tepelnými úpravami. Štrukturálna charakterizácia bola spravená pomocou techniky SEM, TEM a EDX a vyhodnotenie nielen z štrukturálneho, ale aj z materiálového hľadiska. Jedinečná koreňová štruktúra samousporiadaných nanotyčiniek bola vyhodnotená a porovnaná po troch rôznych tepelných úpravách: po anodizácii, po vákuovom žíhaní, a po žíhaní vo vzduchu. Všetky prototypy obsahujú nanotyčinky s amorfnou štruktúrou, ale našli sa však aj nanokryštály pod koreňovými štruktúrami.
Elektrická charakterizácia prototypov ukázala: odporové spínacie správanie (RS), diódové charakteristiky a charakteristiku podobnú pre diódy s kapacitorom. Aktívny povrch pre spínací mechanizmus je v hornej časti nanoštruktúr na rozhraní nanotyčiniek a zlatej elektródy. Výška Schottkyho bariéry na rozhraní Ti / TiO2 bola vypočítaná dvoma spôsobmi a pre všetky tri zariadenia bola nižšia ako 1,11 eV.

KĽÚČOVÉ SLOVÁ

TiO_2, anodická oxidácia, odporové spínanie, Schottkyho bariéra, nanotyčinka, oxid hlinitý

MÁRIK, Marian. Nové nanoprvky pro elektroniku – příprava a charakterizace [online]. Brno, 2021 [cit. 2021-04-30]. Dostupné z: https://www.vutbr.cz/studenti/zav-prace/detail/125711. Dizertační práce. Vysoké učení technické v Brně, Středoevropský technologický institut VUT, Středoevropský technologický institut VUT. Vedoucí práce Jaromír Hubálek.

DECLARATION

I certify that the work presented in this thesis was performed independently, under the supervision of doc.Ing. Jaromír Hubálek Ph.D., and is original with the sole exception of the technical literature and other sources of information that are acknowledged in the text and reference list, and that the material has not been submitted, in whole or in part, for a degree at this or any other university.

Brno ....

(Ing. Marian Márik)

ACKNOWLEDGEMENTS

I would like to thank you to my supervisor doc. Ing. Jaromir Hubalek, Ph.D. for his support during my studies and my work. I would like to thank to my colleagues from LabSensNano for their suggestions and ideas.

Special gratitude goes to Dr. Alexander Mozalev for his advices and for the introduction into the world of electrochemistry. Also, I would like to thank to Dipl.Ing. Maria Bendova, Ph.D., for his support and because she taught me the importance of the data organization and the reporting.

My sincere gratitude goes to my family and friends for their well-timed motivation, they support me always in the biggest needs. Last, but not least I would like to thank you to my wife and to my daughter for their patience and love.

Contents

INTRODUCTION

In 1965, Gordon E. Moor said about the semiconductor manufacturers, they had been doubling the density of components on integrated circuits periodically every second year. His prediction, commonly known as Moor's law, has been fulfilled in the last fifty years. [1.] According to the current state of art, that paradigm eventually comes to the end in the next 5 or 15 years. Instead of the focus just on the size reduction, the electronic industry should emphasis more on the increasingly capable devices. [2.]

The common available memory devices were mostly based on transistor oriented electronic design, which is not limited just with decreasing size and basic laws of physics, but also with suitable combination with passive elements. Introduction of a new passive element, called memristor, could be improving the performance of digital circuits. [2.] Main advantage of the memristors is their ability to save information. The memristor is able to ”remember” the last state before the power is switched off.

Since May 2008, when the research laboratory of Hewlett Packard published the first experimental memristor (Strukov et al., The missing memristor found, Nature Letters [3.]), the interest ain the resistive and memristive research suddenly increased. Based on the state of the art of the memristor technology, the possible way to realize a commonly usable resistive memory is extremely wide. Using an oxide-based multilayers is one of the feasible directions.

This essay is dealing with fabrication and characterization of metal/oxide/metal devices with expected resistive switching abilities, which are basics of memristors for non-volatile memory applications.

The first part of this study is dealing with the fundamental theoretical knowledge about memristors, briefly from mathematical background through the current state of the art continuously to the deeper introduction of the titanium dioxide (TiO_2) based resistive memories. The second part of the thesis is oriented on the practical works and experimental results. The fabrication is focused mainly on the TiO_2 nanostructures, prepared, and modified with electrochemical processes. The electrical characterization of prepared structures is discussed as well.

1 AIM OF THE WORK

Considering the variability of the valve metal oxides preparation and the possibilities of its usage in electronics, the aim of this thesis is to seek a fabrication technique using self-ordered anodic alumina arrays with TiO_2 nanocolumns and investigate its electronic properties.

The particular aims of this thesis are:

- Preparation of the self-ordered AAO supporting matrix with self-grown TiO_2 nanocolumns and realization of the electric contacts for further measurements.
- Investigation of the functional material and the structure analysis of the nanocolumns grown at different conditions.
- Electrical characterization of prepared samples, evaluation of achieved resistive switching phenomenon.

2 EXPERIMENTAL

The fabrication complexity and expensive techniques used for memristor realization in HP lab (written in cap. 2.2) are not very popular in the most of research and industry laboratories. Even their idea is genius it could be further improved. Anodic oxidation of aluminum is a well-known process. This process can produce the porous films possessing high pore density, uniform pore size. The other important advantage is the versatility and low cost. [23.]

In 1999 Mozalev et al. published an article about the microresistors fabricated by anodic processes. [24.] They produced nanoscale metal-oxide coatings, using Ta-Al layers and anodic oxidation. Main advantage was the self-growing of tTa_2O_5 nanostructures with high electrical resistance. Later in 2005, Mozalev et al. also characterized the growth and electrical transport properties of self-organized Ta–Al bilayers formed by anodization. [8.] During the material characterization of the cross-section sample of tantalum oxide nanohillocks in anodic aluminum oxide (AAO or porous anodic alumina PAA) layer, a non-homogenity of the oxygen concentration was detected. Using the information, it might be possible to prepare self-ordered memristive structures via anodization. [25.]

The schematic of the experimental plan (Table 1.) was set up with a purpose to compare different nanocolumn properties and find a way to prepare samples with resistive switching behavior. Samples, where resistive switching is achieved, will be analyzed in detail in electrical and in material point of view as well. If the sample was successfully prepared and it shown resistive switching behavior, the field can be green, if it was successfully prepared, but it is without resistive switching the field will be yellow. In case of failure at the fabrication, the field is red.

Table 1.: Experimental plan

Anodization potential	**Sweep rate for re-anodization**	**Sweep rate for re-anodization**	**Annealing set up**		
	0,2 $V \cdot s^{-1}$	**2 $V \cdot s^{-1}$**	**As-Anodized**	**500°C/2h in Vacuum**	**500°C/2h in Air**
40V					
40V rA 100V					
40V rA 130V					

2.1 Layer preparation

The Ti layers, deposited by PVD evaporation or magnetron sputtering method, are not ideal for template-based anodization. Obviously in the evaporated/magnetron sputtered layers is observable a material stress or the layers crystallographic orientation is not uniform.

The Ion beam assisted deposition is a highly precise sputtering technique which fulfills every requirement of Ti layers for anodic oxidation.

Thermal-oxide-coated Si wafers of diameters 100 mm were used as starting substrates. Titanium layers with thickness 300 nm were deposited by sputtering of 99.95% Ti target, using an ion beam sputtering. The deposition chamber was initially evacuated to $5 \cdot 10^{-7}$ mbar, with subsequent sputtering using 99.998% argon at $5 \cdot 10^{-3}$ mbar. The Ti/Al bilayers (aluminum-on-titanium) were prepared by sequential sputter-deposition of Ti and Al layers, respectively 100 nm (Ti) and 100 to 1000nm (Al) thick.

The wafer was cut on pieces with dimension 1x1 cm and categorized in four groups, based on Al thickness. The rest of the wafer was considered as scrap pieces, with a thinnest Al layer. (Figure 2.1.)

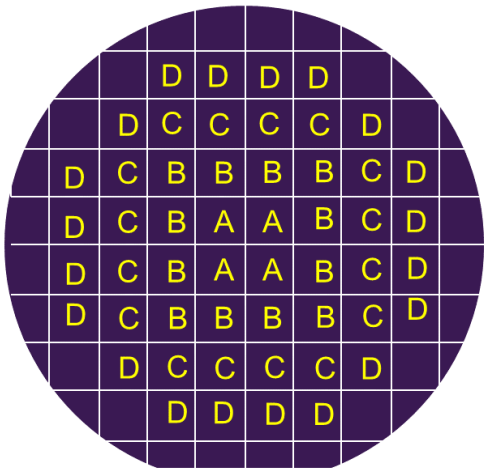

Figure 2.1.: Wafer drawing with marked section groups. The wafer was cutted into 1x1 cm pieces with diamond scratcher.

Based on previous experiences about anodization of sputtered Al layers a non-uniform layer thickness was observed. The thickness differences may cause undesirable inaccuracy mainly during two step anodization, where the precise thickness control during the Al anodizing is obligatory. The different anodization times are presented in Figure 2.2.

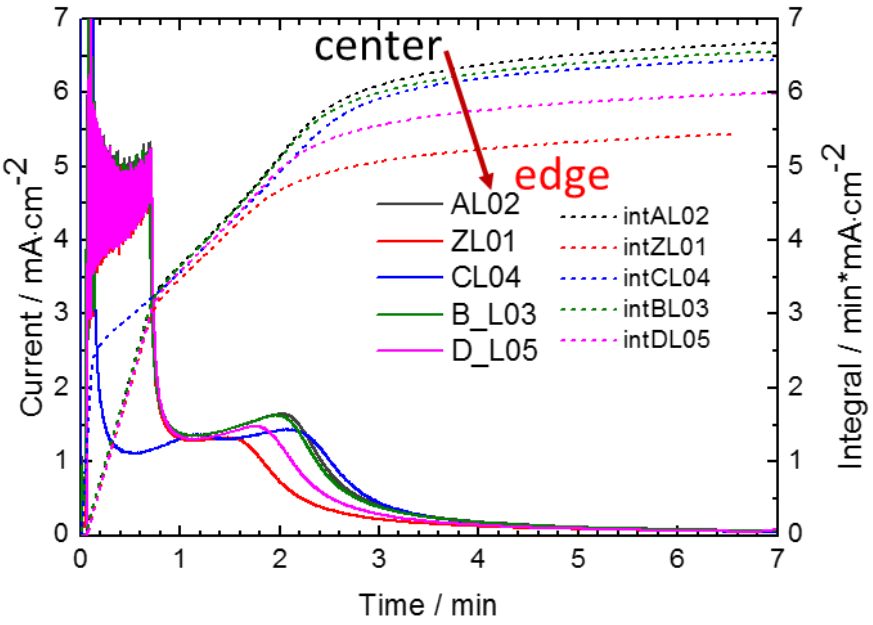

Figure 2.2.: Current time curves of anodized Al layer sputtered by IBAD. Anodization was performed at different wafer positions. The integral of the curves showing clearly, the thickness of the Al layer from the center to the edge is decreasing.

2.2 Anodization of Aluminum

Valve metals as Al, Ti, Ta, W, are specific metals which are suitable for anodic oxidation.

The first part of the experimental work is optimization of the anodic oxidation of Ti/Al structures. The initial surface was sputter-deposited metal bilayer of Ti/Al on the silicon wafer (previously covered with 500 nm of SiO2). Titanium layer with thickness of 300 nm was covered with 550 nm thick Al layer. The anodization was performed at 5 °C with a 0.3 M oxalic acid solution at the circulation speed of 70 mL/min. The apparatus was equipped with poly-tetrafluor-ethylene (PTFE) cylindrical head with internal diameter 6.9 mm equipped with a stainless steel electrode. (Figure 2.3.)

During the anodizing process, the current was always limited to 5 mA and the potential for the aluminum layer was constantly kept at 40 V. The diameter of the pores in AAO is approximately 36-40 nm. The surface of the AAO for more detailed evaluation was chemically decorated with selective AAO etchant. (Figure 2.4.)

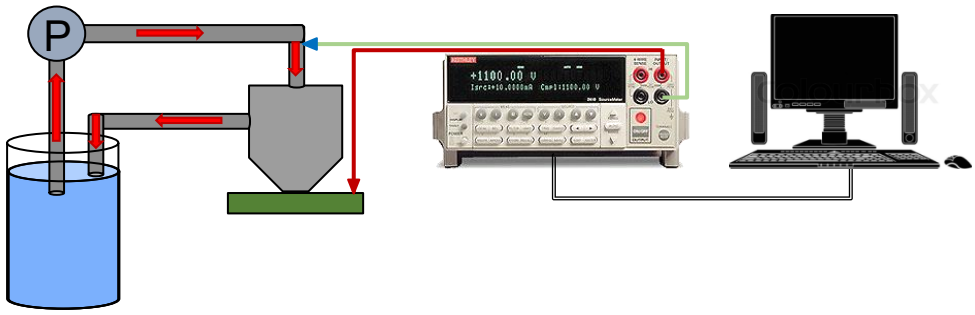

Figure 2.3.: Schematic view of the anodization station.

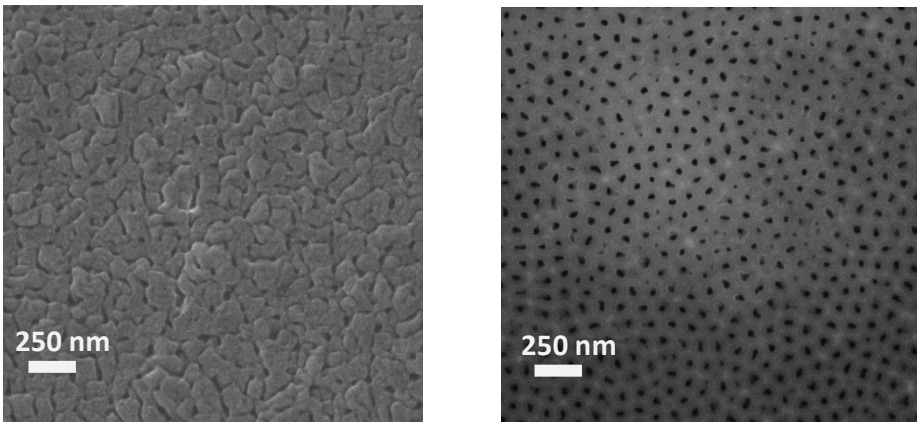

Figure 2.4.: Surface of the AAO template anodized at 40V before chemical decoration (left) and after decoration for 20 seconds (right).

2.3 One step anodization

The first part of the experimental work is optimization of the anodic oxidation of Ti-Al structures. The initial surface was sputter-deposited metal bilayer of Ti/Al on the silicon wafer (previously covered with 500 nm of SiO2). Titanium layer with thickness of 300 nm was covered with 550 nm thick Al layer. The anodization was performed at 5 °C with a 0.3 M oxalic acid solution at the circulation speed of 70 mL/min. The apparatus was equipped with poly-tetrafluor-ethylene (PTFE) head with internal diameter 6.9 mm equipped with a stainless steel electrode.

During the anodizing process, the current was always limited to 5 $mA \cdot cm^{-2}$ and the potential for the aluminum layer was constantly kept at 40 V. The diameter of the pores in AAO is approximately 40–50 nm.

Anodization of the titanium layers were provided at potential of 40 V and 60 V (see Figure 2.5.). Both potentials are suitable to prepare self-grown TiO_2 nanowires in AAO, the difference is in height of TiO_2 nanowires in the pores. At the potential of 60 V the TiO_2 columns are higher than at 40 V. The thickness of the AAO has no influence on the length of the nanocolumns. (Figure 2.6.)

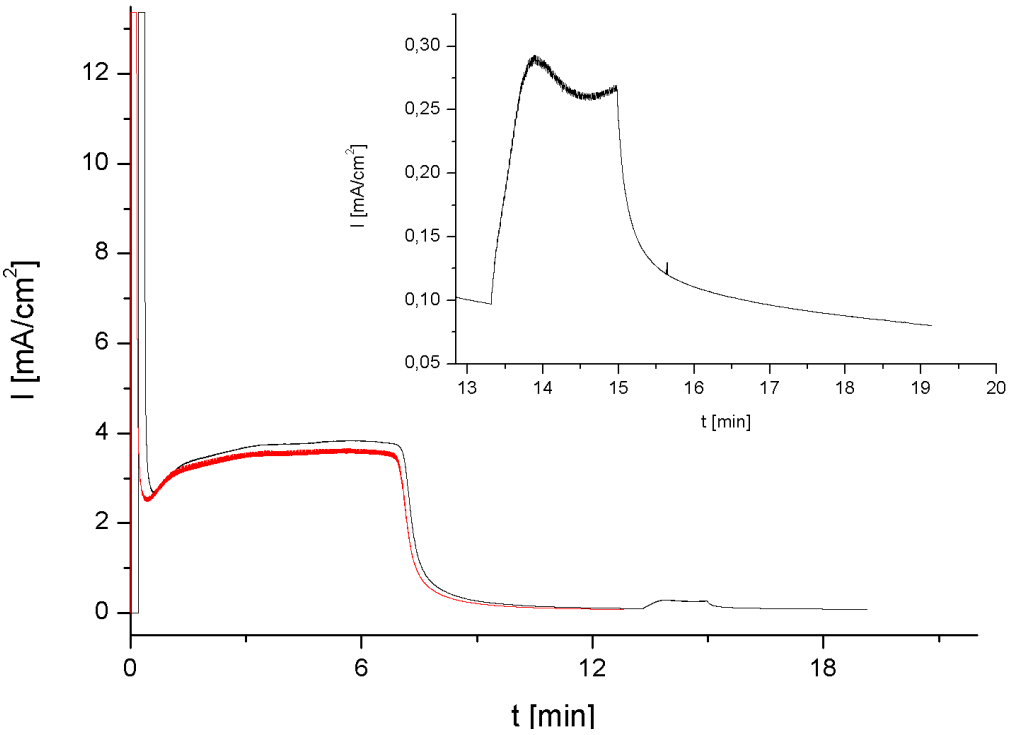

Figure 2.5.: Anodization curve for Al/Ti bilayer. During the anodization of Al, the voltage was kept at 40 V for both sample (red and black curves). The first sample was anodized for 13 min including Ti anodizing at 40 V (red curve). The second sample was anodized for 19.25 min. In case of the second sample after 13.5 minutes the voltage was increased from 40 to 60 V (black curve)

After the first successful and repeatable test the anodization parameters and the type of the samples for comparison purposes were fixed.

The temperature of the electrolyte for the anodization was fixed for 5°C, the flow rate of the electrolyte in the cylindrical PTFE cell was fixed for 70 ml. The anodization voltage for the aluminum layer and for the titanium oxide bulks was constant as well (40 V).

Three column length respectively anodization potential was fixed too. For the shortest column length 40V was used and for higher nanocolumns 100V were applied.

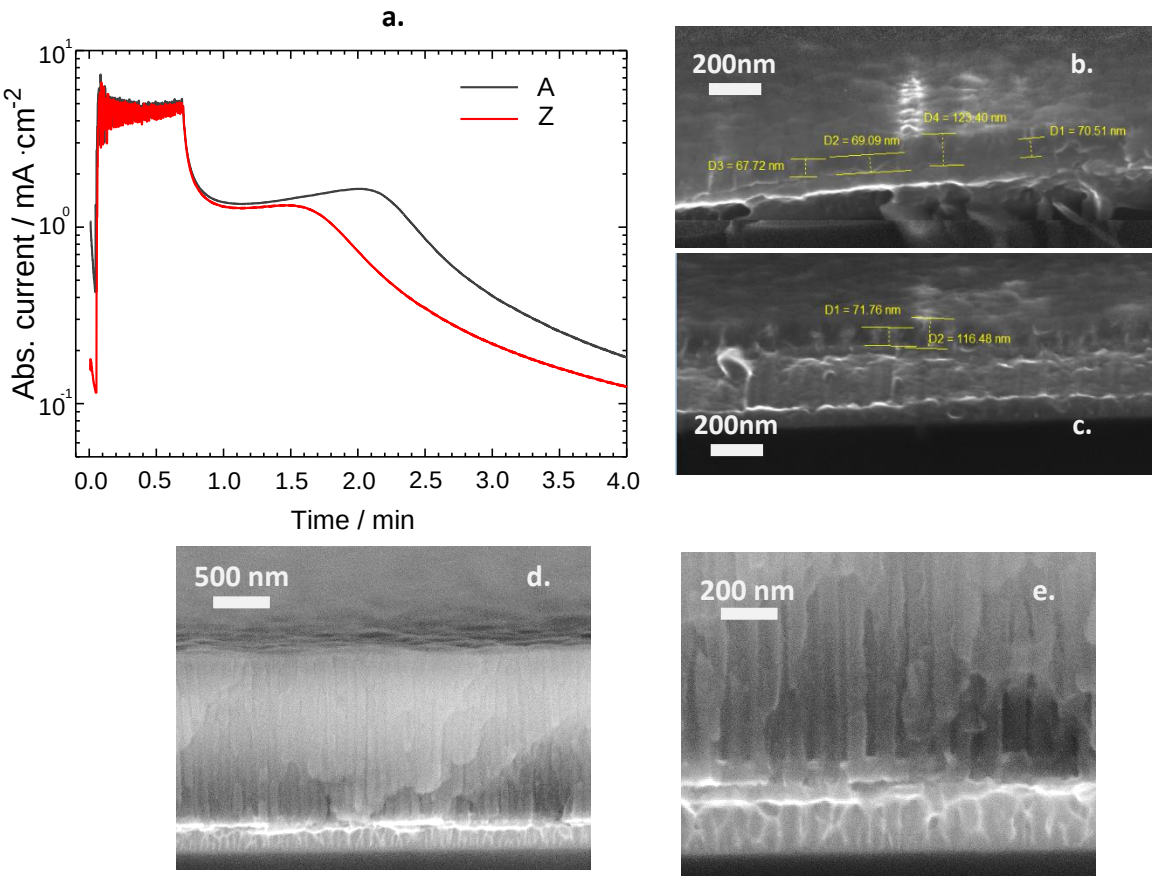

Figure 2.6.: Anodization of an 80 nm thin Al layer at potential 40 V and re-anodized at 60V. The current time curve shows the difference between the anodization time of the Al layer at the center of the wafer and on the edge (the re-anodization part of the curve was removed for better visualisation). The differencies in the final AAO layer thicknesses are approximatley -6 % at the edge in comparison with an anodized center. The re-anodized nanocolumns are about 70 nm.

The figures d and e are presenting an AAO prepared from 1000nm thick Al layer. The final AAO layer is extremly thick in comparison with tha layers in figures b and c, however the height of the nanocolumns are about 70nm, which means the thickness of the AAO has no influence on the growing process of the TiO_2 nanocolumn arrays.

2.4 Two step anodization

In previous chapter the one step anodizing and re-anodizing process was explained. The two-step anodization from the electrochemical point of view is like the one step anodization. The main difference lies in the way of the AAO control. Due to the physical limitation of the AAO growing mechanism, the layer thickness control is possible only with removement of the undesirable layer thickness.

Differences between the final AAO thickness and the initial AAO thickness is depending on the length of the nanocolumns. The height of the nanocolumns is controlled by the re-anodization potential and the initial thickness of the AAO was counted by equation *20* written in chapter ***Error! Reference source not found.***. The calculation was verified with several thickness measurements from cross sections after the anodization. The samples were marked from the back side with dentification sign showing from which part of the silicon wafer was the sample taken. The distribution of the samples was explained in previous chapter 2.1. *Layer preparation*. The samples from the same bar have identic thicknesses and the undesirable layer thickness is definable precisely and easily.

The thickness of the consumed AL layer and the time of the anodization to reach the proper thickness of the undesirable layer specified as $6{,}5 Å \cdot s^{-1}$. The anodization of the aluminum was performed with identic setup for all experiments and therefore the speed of the Al layer consumption was in every case the same.

The process of anodization and the process of chemical etching of the AAO before the second anodization step is provided in the same anodization cell without dismounting. Rinsing of the AAO surface after the anodization was done by constant circulating of demineralized water (200 ml of H_2O at room temperature for every rinsing respectively). The selective etching process with tempered etchant to 58°C at constant circulation for 20 min at speed 75ml/minute was implemented. The selective AAO etchant for the AAO decoration and for the removal was the same. The etching was finished with rinsing to remove the etchant residues from the surface.

Second step of the anodizing process was performed in an identic way as the one step anodization. The results of the two-step anodization are presented in figures Figure 2.7., Figure 2.8.

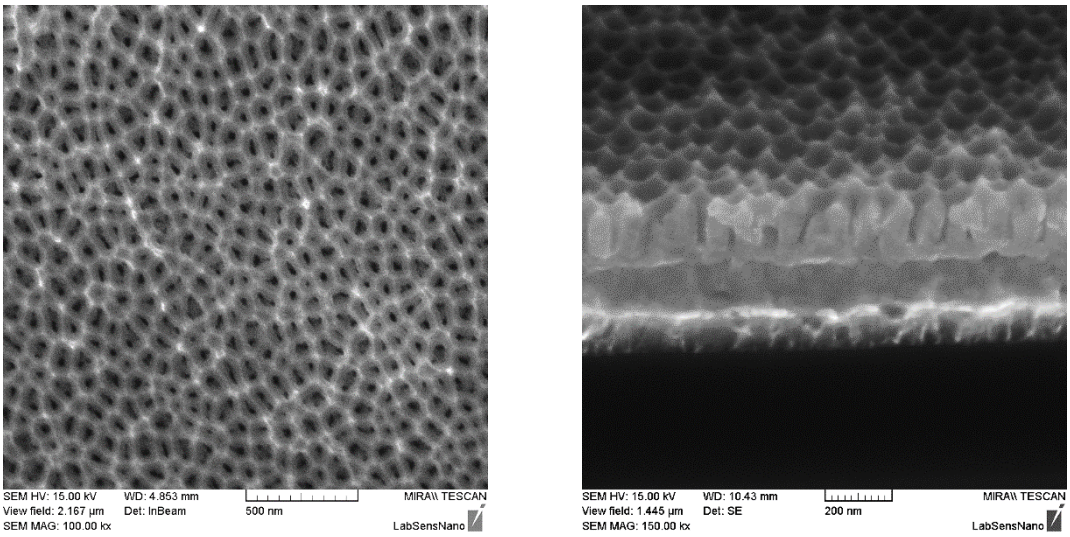

Figure 2.7.: AAO surface (left) after the second anodizing before re-anodization of Ti. Tilted cross section (right) about the AAO template before re-anodization of Ti. After a re-anodization the pores should be filled with TiO_2. The not completely flat AAO surface has no negative effect on a later magnetron sputtering or on the electrical contacts.

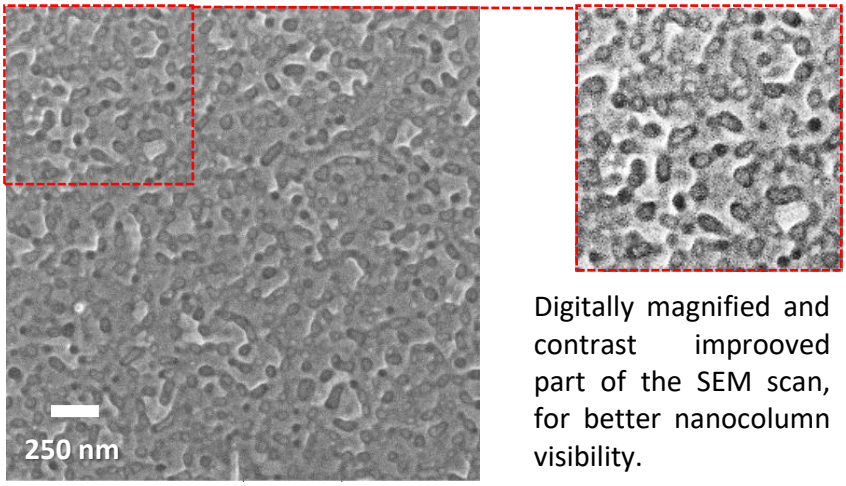

Figure 2.8.: Surface of a re-anodized AAO template prepared with two step anodization. The surface was decorated in selective AAO etchant for 20 seconds for better visibility. The top of the nanocolumns are clearly visible.

2.5 Anodization of Titanium

The anodization of the Ti layer in aqueous oxalic acid solution with sequential anodizing technique was realized. The anodizing process of the Ti layer is starting with the formation of the TiO_2 nanodots at the bottom of the AAO pores on the barrier layer. The speed of the anodic reaction at constant voltage is depending mainly on the electrolyte temperature. Higher is the temperature, the reaction is faster. At higher electrolyte temperature the oxidation process is faster than the growing speed, therefore the nanostructure can be instable and dissolve during the anodization causing a breakthrough across the layer. Due to this phenomenon after several experiments 5°C was chosen as an electrolyte temperature.

Titanium ion migration through the AAO barrier layer is depending on the temperature, on the anodization potential and current. Basic column, which is a titanium dioxide column anodized at potential 40 V as an AAO was prepared, has two main parts, the root and the column itself.

The Ti4+ ion migration through the AAO barrier layer are leading to a growing mechanism. Higher anodic potential leads to a better anodic titanium oxide (ATO) growing and the AAO nanopore filling redounds ATO nanocolumns. However, the anodizing process results titanium oxide growing, also an inward O_2 ion migration appears on the interface of the AAO barrier and Ti layer. (Figure 2.9.)

The I–t curves from the anodization process were presented in chapter 1.3, where the correlation between the anodization time and the AAO thickness was shown. To control how many pores are filled with nanocolumns, the AAO was removed. The pore saturation is around 95 to 100%. (Figure 2.10.) After a partial AAO removal the nanocolumns becomes visible, however the most of the nanocolumns were felt down or removed after a full template removal.

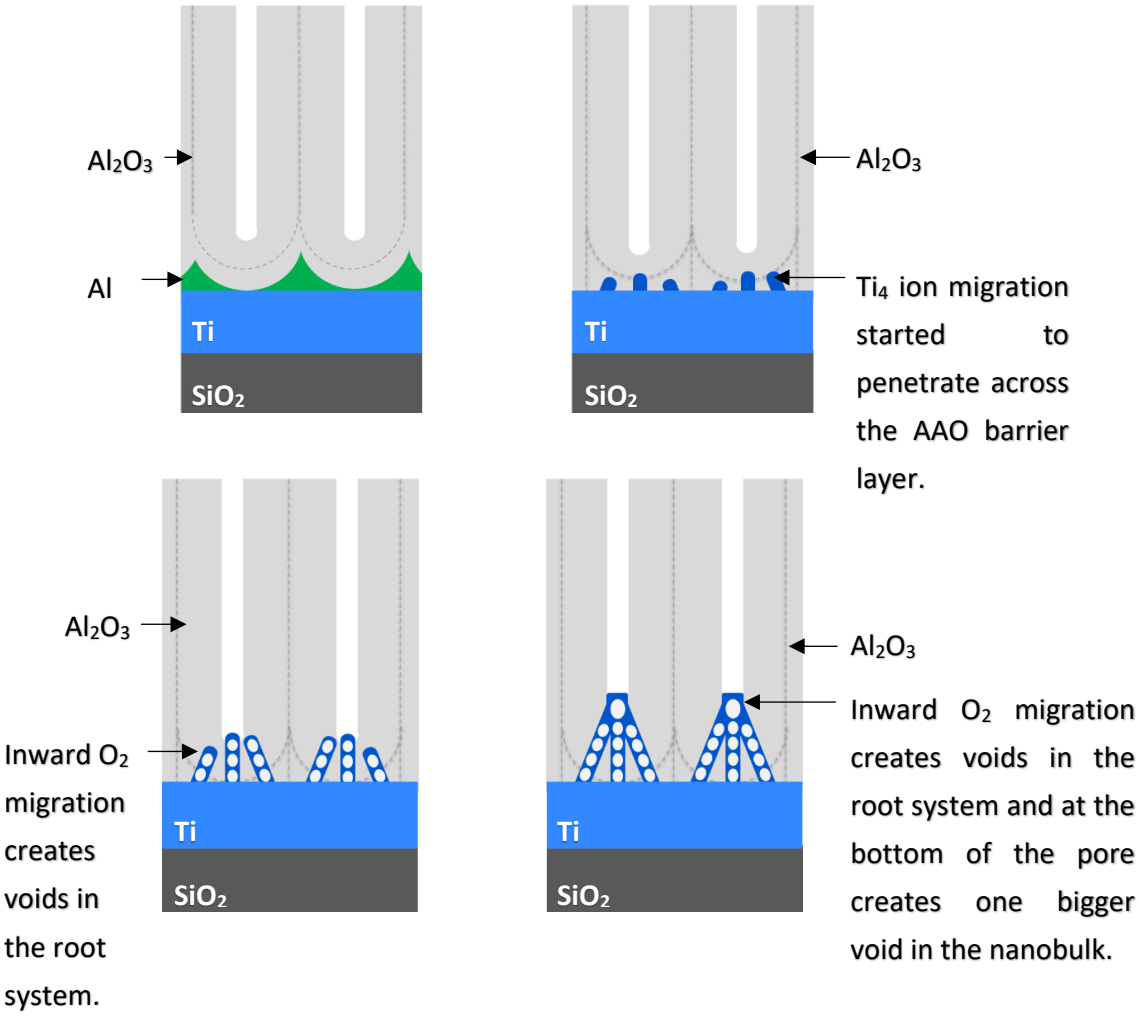

Figure 2.9.: Schematic view of the TiO_2 growing through the AAO barrier layer at potential 40V. During the anodization at first all of Al is anodized (a.), then the Ti starts to penetrate through the barrier layer at the thinnest places respectively at the places with a lowest resistence.(b) The inward O_2 migration creates voids in the stems and later in the cap on the nanocolumn as well.(c., d.)

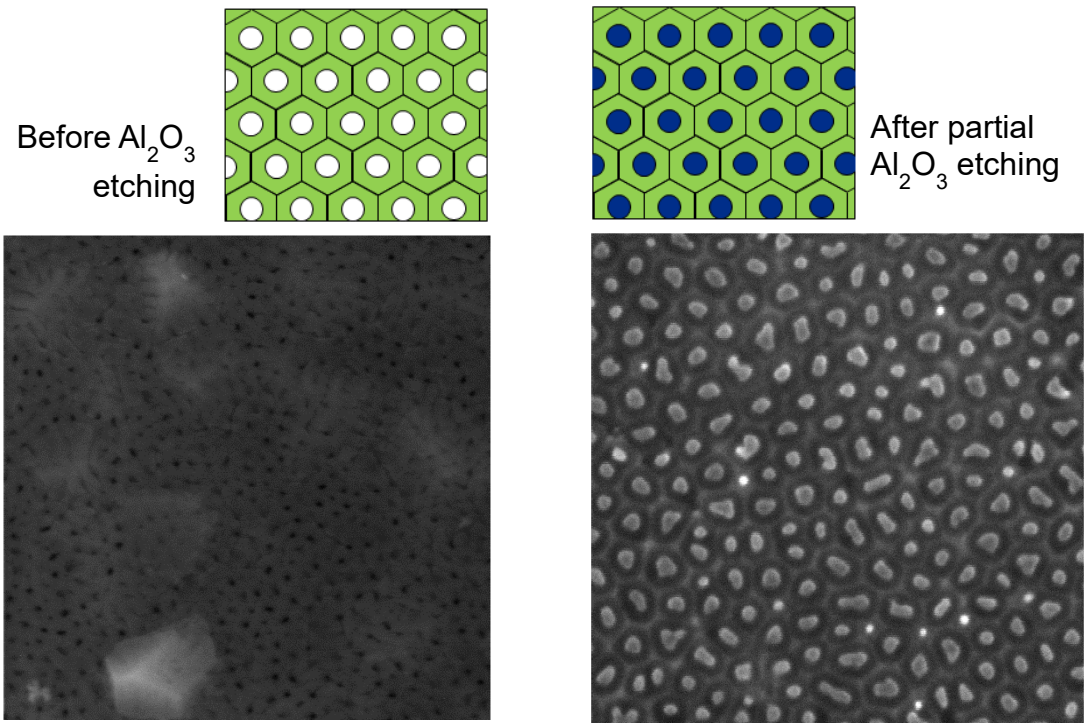

Figure 2.10.: The pore saturation was controlled by a partial AAO removal. The surface of the AAO after the re-anodization (on left) before decoration, and the nanocolumns in the partially removed AAO template (on right). To see the effectivity of the saturation in detail, after an AAO removal only a part of the surface is shown.

The negative effect of the voids, besides the nanocolumns are not stable after AAO removal, is the possible lentil surface during the anodization. Where the sample was ruptured or over-burned due to the high current density in a local point. Based on these experiences at anodic oxidizing we initiate higher amount of O_2, migrating into the barrier layer. The shape of the roots and amount of the root filaments are changing simultaneously. During a long time finishing the voids are merging filling up the barrier layer. Later, the voids are spreading above the Ti layer and breaks up the AAO template. (Figure 2.12. Figure 2.12)

Re-anodizing sweep rate at reaching of the final re-anodizing potential has influence on the grown speed and on the electrical properties of the columns as well. This chapter briefly explain the differences in the grown process at sweep rate difference from 0,2 $V \cdot s^{-1}$ to 2 $V \cdot s^{-1}$.

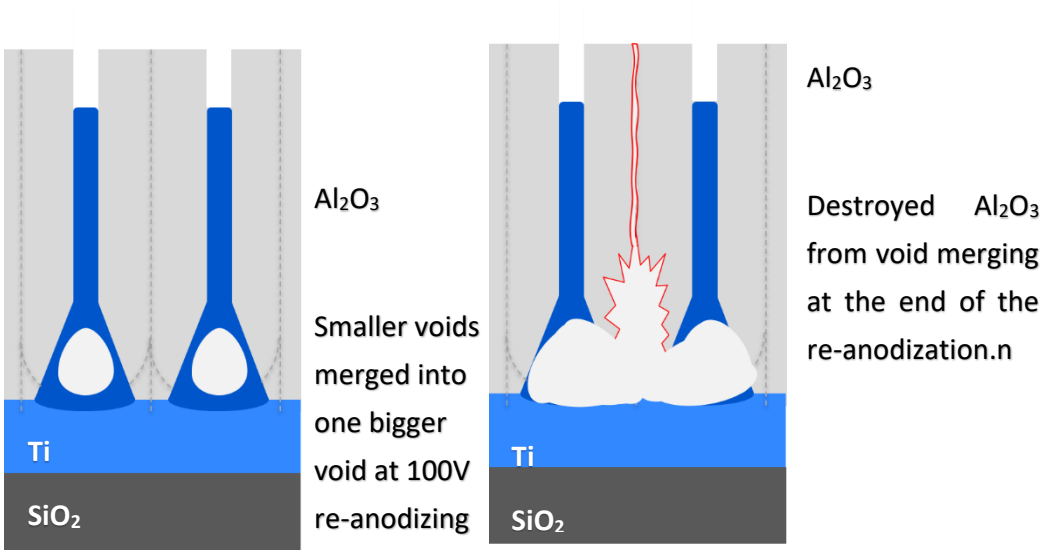

Figure 2.11.: The re-anodization at potential 100V reached at slow sweep rate leads to long nanocolumn growing, but the inward O_2 migration, respectively the voids in the nanocolumn in the AAO pores are not present. The root system in the AAO barrier layer due to the re-anodization is changing its structure. The voids from the O_2 migration are fulfilling the barrier layer and transforms the stem structure into one flask shaped root with 1 to 3 voids. (left) The long-time anodization finishing leads to a void merging between the roots and to a layer destruction. (right)

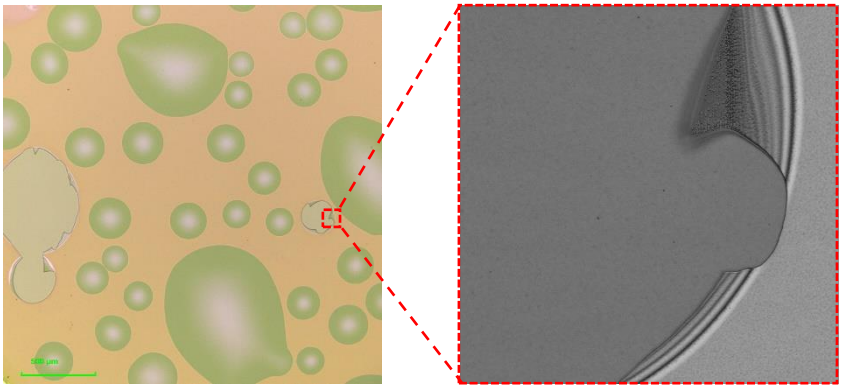

Figure 2.12.: Lentil like damage on the AAO layer caused by long finishing anodization. (left) The magnified damage after eruption is magnified on a laser scanned image (right)

The nanocolumn grown speed is higher and the final nanocolumns are about 10% higher than at lower speed. If the growing process is faster the inward O_2 ion migration is causing bubble merging slower than at lower sweep rate. The nanocolumn can be anodized at higher potential as well (at 130V without any AAO damage).

The different grown speed assuming different material or root structures and electrical properties respectively.

The differences in low and high sweep rate are presented (Figure 2.13), where the anodizing charts are explained the growing phases are illustrated.

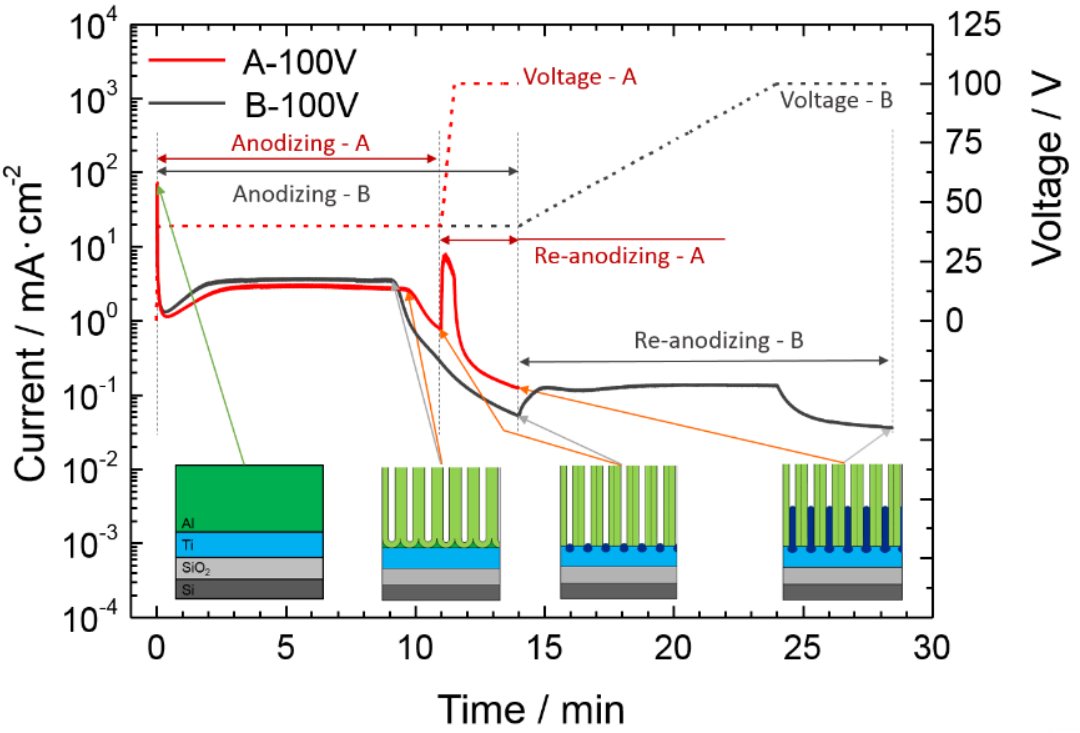

Figure 2.13.: Comparison of sweep rate of re-anodizing potential. Current-time and potential-time transients recorded during the AAO-assisted anodization of arrays A-100V (red) and B-100V (black). The different regions (anodizing and re-anodizing) are marked and the images show schematically the arrays at the corresponding current or potential changes.[43.]

2.6 Deposition of top electrode arrays

This chapter is dealing with the fabrication of the metal contact pads of TiO_2self-ordered nanoarrays for electrical characterization. The bottom electrode of this two-terminal element is the Ti layer itself. The highly conductive pure metal layer is perfectly connected with the nano column array and it is easily accessible from the side of the chip.

The top electrode material based on the literature should be a noble metal, as platinum or gold layer. Regarding to the available techniques and sources electrochemically or magnetron sputtered gold layers were chosen. The magnetron sputtering of Au was performed at standard set ups (prepared in CEITEC Core facilities in form of order) and therefor only the electrodeposition will be discussed in detail.

The AAO surface before deposition was decorated for 10second with *AAO etchant,* later on rinsed in demi water and dried with hot air at 80°C for 2 minutes. The clean and dry micro channels are obligatory for a successful electro-deposition. Every contaminant decreasing the deposition quality and distorting the results form later electrical characterization. The back side and the edges of the chip were isolated by a nitrocellulose-based polymer (nail polish).

The electrolyte tempered for 45°C was stirred in an open electrochemical cell with gold counter electrode. The distance between the working and the counter electrode was 4mm. The continuous stirring serves to keep stable temperature and a constant amount of gold ions above the working electrode.

Deposition set up for pulsed galvanostatic method:

Electrolyte:

- 0.183g $K[Au(CN)_2]$ + 250ml H_2O
- T = 45°C
- Stirring = 300rpm

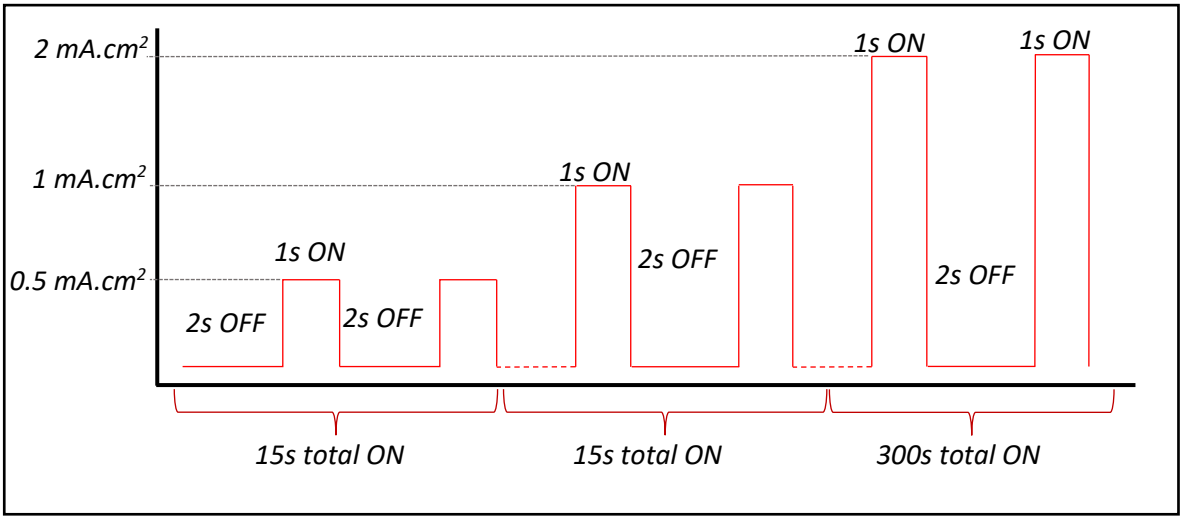

Figure 2.14.: Schematic view on the deposition set up for Au electrodeposition into AAO.

During the deposition three different current pulse limits were used with length 1 s and with relaxation time 2 s after pulses in all cases. The first two low limits serve for soft deposition starting. At low current limit in the pores a very thin gold basic layer can grow. In case of the third current limit, when the electric potential is moving between 3 to 20 V the pores are fulfilled with gold and on the top of the chip is covered by a homogenous gold layer. Stabilization of the top electrode was performed with a 10min long heat treatment at 200°C on a hot plate.

2.7 Material and structure characterization

Electrochemically deposited TiO_2 nanoarrays were analyzed and characterized in detail. Every small change in the preparation set up has direct effect on the self-grown nanocolumns material structure. In next chapter the characterization and the growing process will be written.

Main techniques for layer characterization were chosen SEM, TEM observation and EDX material analysis. SEM microscope Mira II LMU and Lyra 3 from Tescan Orsay holding was used. During SEM analysis the previously cleaned and in case of cross sections chemically decorated samples were observed by SE and InBeam secondary electron detectors were used at working distance 1 to 8 mm with acceleration voltage 15 to 30kV. The sample surfaces were not deposited by a conductive layer before the SEM analysis.

Chemical decoration was provided by a selective aqueous highly toxic etchant 0.6 M H3PO4 and 0.15 M CrO3) at 60 °C respectively for 5 to 20 seconds. The selective AAO etchant in a short time etches the AAO surface and at cross sections the walls of the AAO pores, therefore the contrast between the TiO_2 nanocolumns and the AAO is improved

The TEM samples were prepared on FEI Helios FIB/SEM microscope and analyzed on FEI Titan transmission electron microscope.

Observation, analysis and evaluation of selected samples were subjected to fast furrier transform (FFT) analysis for determination of crystallographic orientation in the columns, roots, AAO matrix and in pure Ti layer as well.

FFT imaging and final image processing was performed by software FEI TEM Imaging and Analysis ver. 4.14.

EDX investigations were performed by a high sensitivity FEI Super-X detector. The observed are was scanned with a with the 300 kV electron beam and using a beam current of 0.15 to 0.5 nA, dwell time of 20 µs, and a spot size 0.3 to 1 nm. The thickness of the lamella under the observed surface was always about 50 nm or lower.

Quantitative evaluation of the data was completed with FEI software Velox version 2.2.1. Over selected parts of the anodic films and within the lines along selected nanocolumns a data integration was performed.

2.7.1 Material characterization by TEM and EDX

The structure of the AAO layers was written in previous chapter. Regarding to the same preparation conditions of the AAO templates in every case, the barrier layer properties are considered constant for all experiments.

Anodization of the Ti layer starts , when the barrier layer of the AAO matrix reaches the top of the Ti layer.

Titanium ion migration through the AAO barrier layer is depending on the temperature, on the anodization potential and current. Basic column, which is a titanium dioxide column anodized at potential 40 V as an AAO was prepared, has two main parts, the root and the column itself.

Everything between the pure titanium layer and the bottom of the pore is considered as a root. (Figure 2.15.) In current case the characteristic root stems are penetrated through the barrier layer. Number of the root stems is obviously depending on the anodization potential and on the barrier layer properties, such as thickness, surface of the bottom of the pore, etc.

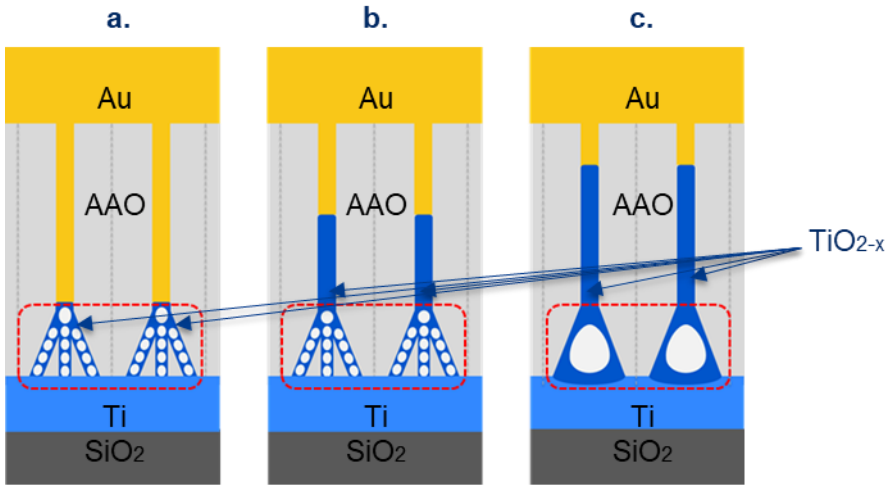

Figure 2.15. Schematic of the nanocolumns at different anodizing potential: 40V (a.), 60V (b.), 100V (c.). The roots are marked with dashed red line.

Various possibilities of using of TiO_2 nanocolumns sensor or photovoltaic techniques motivated to observe columns after the AAO removal. The AAO was removed by selective chemical etchant at 58°C and the column field was observed by SEM. After AAO removal there were no nanocolumns visible on the surface. This is because of the nanoroots that connect the columns with the bottom Ti layer are undergo a modification during the re-anodizing, owing to the oxygen evolution followed by creating of nano-bubbles and voids, and grow as an alumina contaminated TiO_2 nanoroots in the barrier layer. This small amount of alumina in root walls and the extremely thin wall thicknesses next to the voids caused 100% column devastation. We can consider the pure titanium layer is not suitable for mechanically stable AAO less TiO_2 arrays grown by anodic oxidation technique. More detailed information about the mechanical stability was published in article *Influence of*

*nitrogen species on the porous-alumina-assisted growth of TiO_2 nanocolumn arrays (Bendova, Kolar, **Marik** et al).*

The shortest and the longest nanocolumns anodized with one step anodization at 40V (shorter) and re-anodized at 100V (longest) and annealed for 2h at 500°C in vacuum were investigated in structural and material point of view. The nanocolumns re-anodized at 100V without annealing (as-anodized) and air annealed were observed as well.

Crystallographic orientation in different materials was measured in TEM by fast Fourier transform (FFT) analysis, results were evaluated by FEI software TEM Imaging and Analysis version 4.14. Diffraction images are showing local crystallographic orientation. (Figure 2.16.)

In case of Si wafer and Ti layer the results were compared with the wafer datasheet and with results from Gablech et.al. [78.] about preparation of (001) preferentially oriented titanium thin films by ion-beam sputtering deposition on thermal silicon dioxide.

The p-type Si substrate with orientation (111) was observed as a first. The diffraction image shows the perfect (111) orientation. The thermal oxide layer followed the substrates crystallographic orientation.

The Ti layer sputtered by IBAD shows (001) orientation and the AAO was completely amorphous.

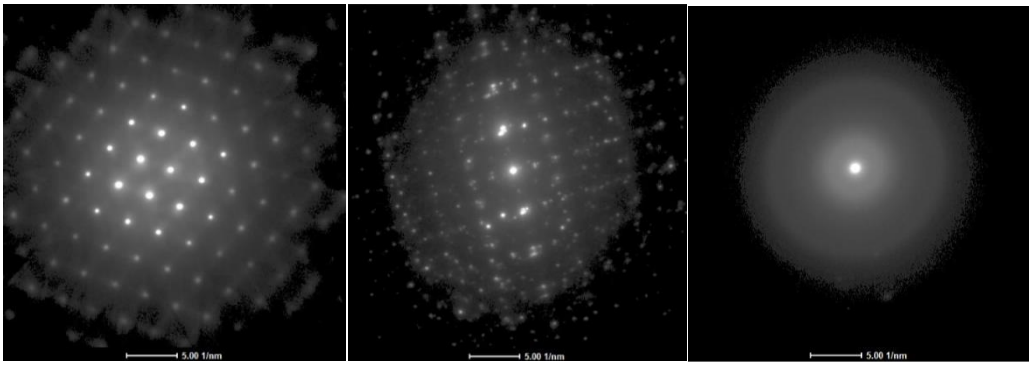

Figure 2.16.: Crystallographic orientation in silicon wafer (111) (a.), in sputtered Ti layer (001) (b.) and in AAO [amorphous](c.) was measured in TEM by FFT analysis. The AAO kept their amorphous character after annealing in vacuum and in air as well.

2.7.2 Characterization of nanocolumns anodically grown at 40V

The root structure at anodization potential 40V is non-homogenous. The root system contains one main stem at the bottom of the pore, where the barrier layer has the smallest thickness and 2 to 5 side stems. The stems are full of voids (full of nano-bubbles), which has significant influence on the column stability after the AAO is removed. The thickness of the stem walls next to the voids are about 1-2 nm. The diameter of the main stem is about 9 to 10 nm, and the side stems are 4 to 6 nm in diameter. The length of the stems is depending on the AAO barrier layer thickness, which is about 36 to 40 nm. (Figure 2.17.)

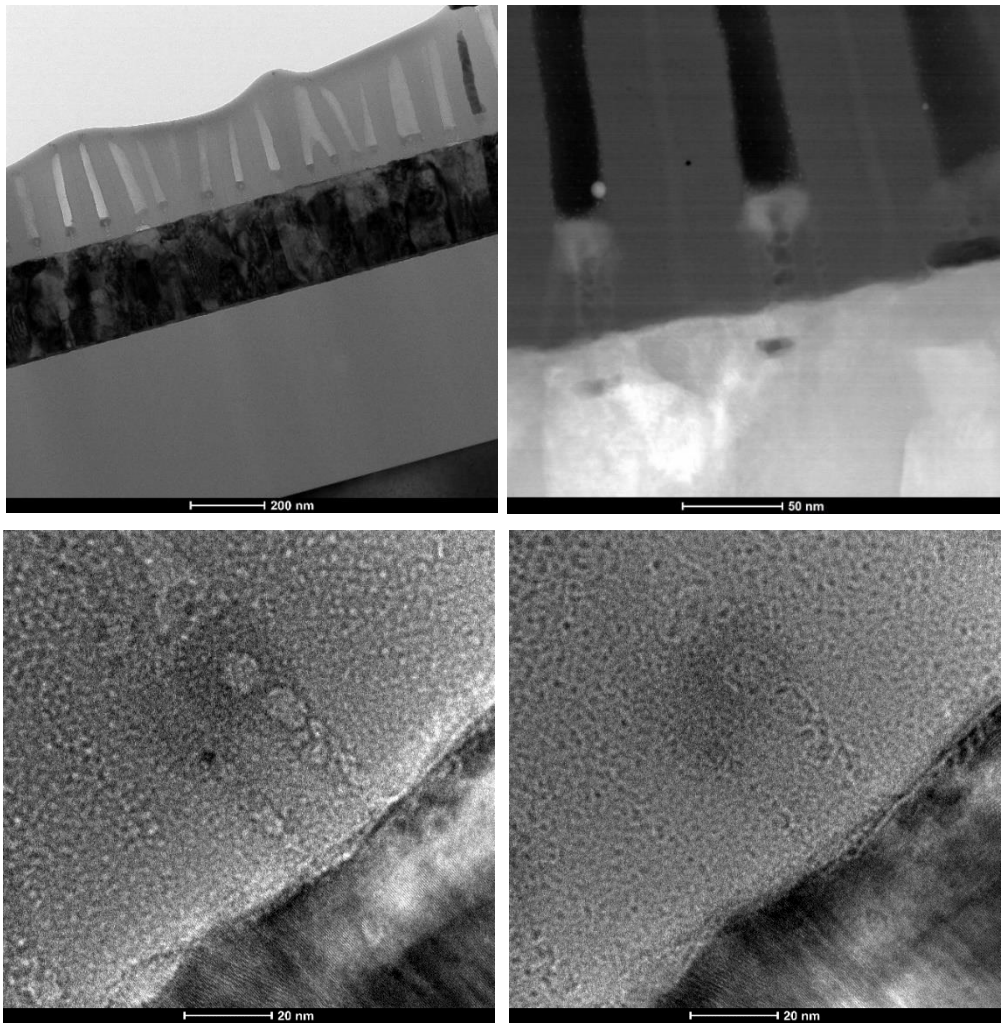

Figure 2.17.: Wide field scan with TEM about the nanocolumns in AAO. One nanopore obviously contains one nanocolumn, but rarely a nanopore can be divided in two sub pores or two pores can merge during anodization as well. (a.). Magnified view on a short nanocolumn with root system contains void full stems. (b.) Verifying of voids with under and over focusing of the electron beam during the column observation. With under focusing the surface and with under focusing the edges are visible.

The TiO_2 nanocolumns were studied using FEI Super-X detector by scanning a selected nanocolumns from the lamella with the 300 kV electron beam. To achieve the best scanning parameters a beam current of 0.15 to 0.5 nA was used with dwell time of 20 µs, and a spot size 0.3 to 1 nm.

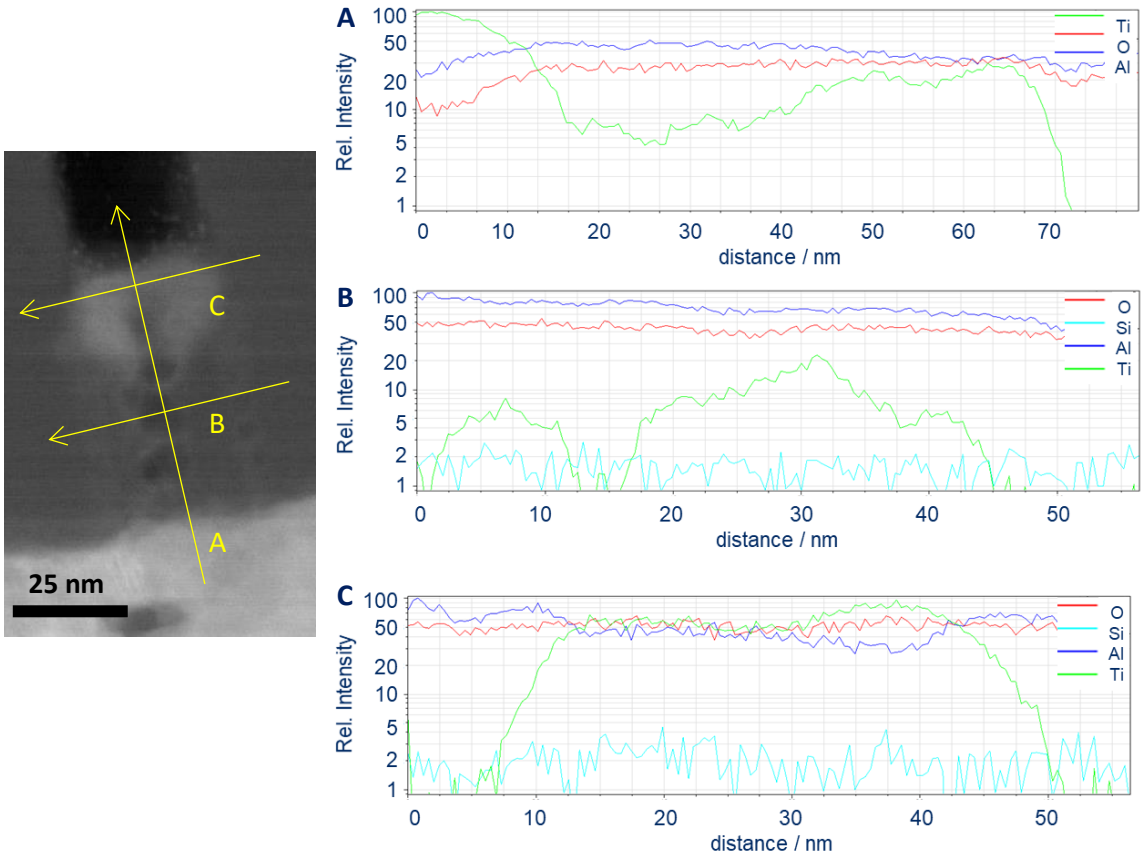

Figure 2.18.: EDX line scans performed on the TiO_2 nanocolumns at three different positions. The line A dealing with a nanocolumn material structure from the Ti layer to the AAO pore. Line scans B and C were collecting material information though the nanocolumns root system (B) and through the top of the column (C).

The EDX line scans about the 40V sample presents distribution of Ti in the nanocolumn. (Figure 2.18.) The results from a vertical analysis are showing non-homogenous distribution of Ti in the root system. The Ti penetration scheme through the AAO barrier layer during anodization was influenced by the electrical resistivity and by the mechanical properties of the barrier layer. Lower resistivity allows better growing possibilities of the TiO_2. Closer to the top of the barrier layer the amount of the Ti in the root system is increasing. The edges of the TiO_2 in the barrier layer during the anodization may slightly mix with an AAO. The O_2 inward migration is visible on the line scans too.

The horizontal scans about the root system are presenting three or four stems, where the middle stem with a bigger diameter, about 22 nm, can be considered as a main stem. The side stem on the left side with diameter appx. 11 nm is clearly separated, however on the right side the stem is close to the main stem and it is slightly backwards. The fourth

possible stem can be placed at position 16 to 24 nm in the line scan, because the Ti line is not continuously decreasing, however the stem on the TEM figure is not visible.

The EDX elemental maps of Ti, O, Al are presented as well. The roots of the nanocolumns are shown amorphous character in as-anodized, in vacuum annealed and in air annealed condition as well. The amorphous character of the nanocolumns on the HR-TEM image is corresponding to the FFT image. The (001) oriented Ti layer confirmed by FFT image is visible under the nanocolumn on the HR-TEM image.

The EDX elemental maps are corresponding to the line scans. The distribution of the Ti in the barrier layer confirms the root structure. Due to the small stem wall thicknesses and the anodizing conditions the AAO and TiO_2 mixture in the walls is possible. Additional oxide layer under the nanocolumn and between the border of the Ti layer was not observed by HR-TEM and neither by EDX elemental maps. (Figure 2.19.)

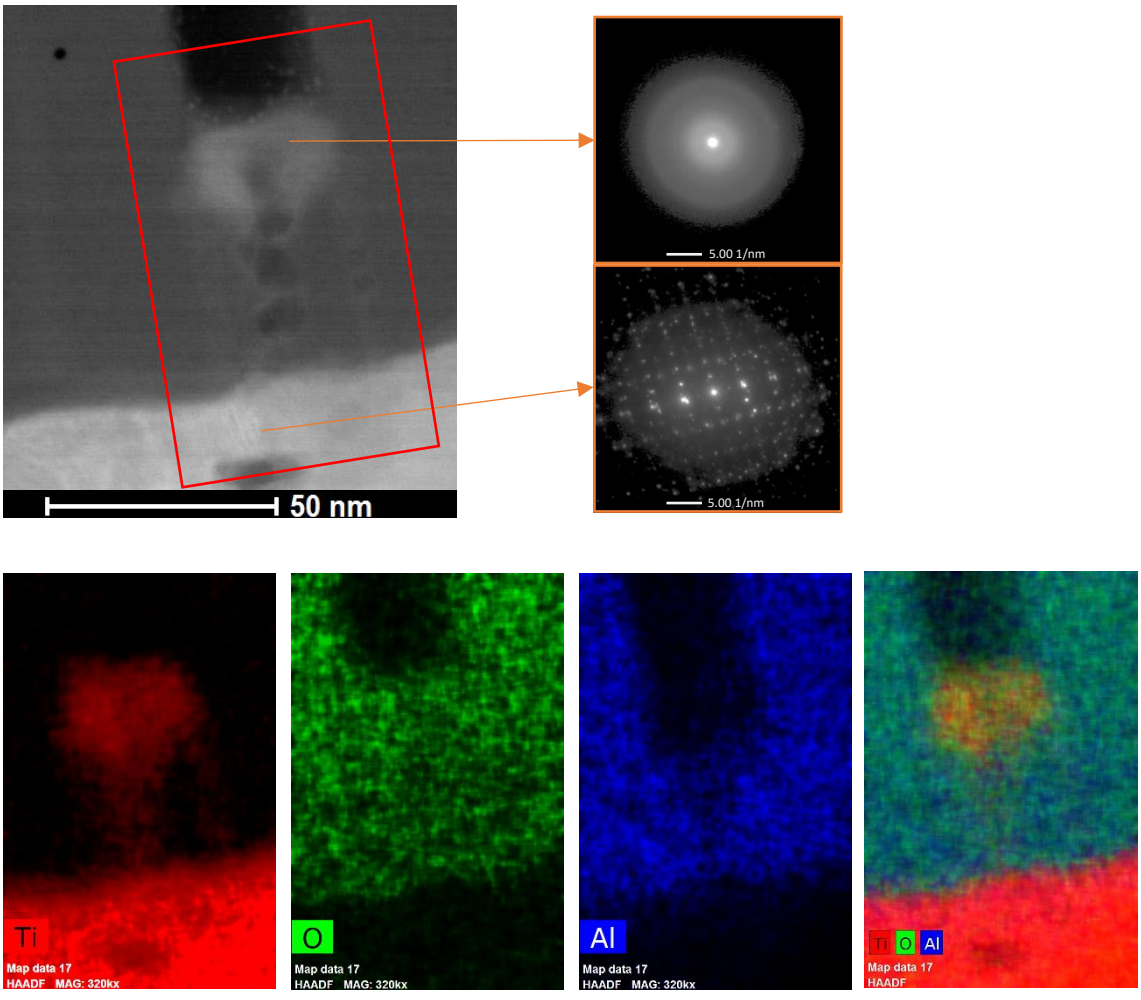

Figure 2.19.: EDX elemental maps about the nanocolumn anodized at 40V. (b,c,d,e) On the HR-TEM image (a) in the Ti layer a crystallographic orientation is visible and it was confirmed by FFT(g). The top of the nanocolumn has amorphous character (f) similarly to the AAO.

Electrodeposited gold was observed by HR-TEM and EDX as well. The nanopore is filled perfectly, the gold filling is homogenous without voids or cracks. Between the top of the nanocolumn and the electrodeposited gold is direct contact overall the TiO_2 surface. EDX line scan from the Ti to the top of the Au column was investigated. The results of the analysis proved the TiO_2 nanocolumn is not mixed with the Au column. In the line scan approximately from 85nm to 95nm the elemental lines are covering each other. This phenomenon is caused by a convex shaped top of the nanocolumn. The convex shape of the column is used to be visible on the HR-TEM images, if the TEM lamella is polished through the nanocolumn. (Figure 2.20Figure 2.20.)

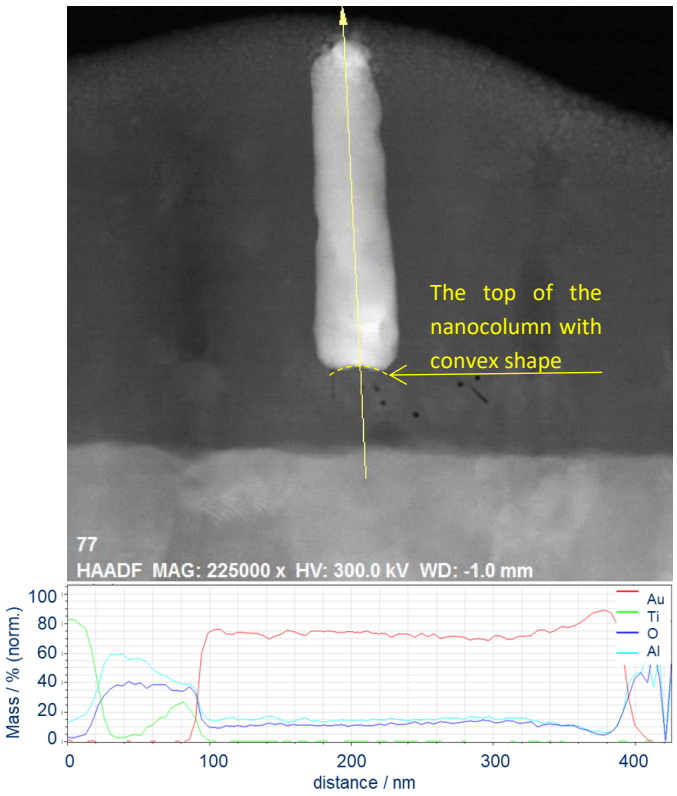

Figure 2.20.: EDX line scan overall the nanocolumn and the electrodeposited gold column. The convex shape on the top of the nanocolumn is marked with yellow dash line.

2.7.3 Characterization of nanocolumns re-anodized at 100V

HR-TEM observation shown significant differences between samples anodized only at 40V and samples re-anodized at 100V.The growing mechanism of the AAO was already written above and published as well by many researchers, as Mozalev, Habazaki, etc. The growing mechanism of the TiO_2 nanocolumns in presence of water based oxalic acid solution brings several changes in column structure, especially in root structures.

From top down view the column structure in AAO pore is homogenous, the length of the column depends mainly on applied potential. The higher is the potential, the longer are the columns.

Re-anodization increases the column length about $1.6nm \cdot V^{-1}$ of re-anodization potential (re-anodization at 100V = 40V basic potential + 60V re-anodization potential with sweep rate $0,2V \cdot s^{-1}$).

The top $\frac{2}{3}$ of the column length is a void less amorphous $TiO_2 + TiO_{2-x}$ combination where the Oxygen content increases in the direction of the surface.

The bottom $\frac{1}{3}$ contains low number of smaller voids penetrated from the root into the column.

The root structure due to re-anodization is transforming into a simpler structure. The stems are obviously missing, with higher potential the stems are merging, the voids are expanding and merging as well, and it lasts until the main root contains 1 to 3 bigger voids with width about 65 to 70 nm. If the re-anodizing potential is too high, the voids expands through the AAO sides and they merge into bigger bubbles, which destroys the AAO layer.

The nanocolumns re-anodized at potential 100V without annealing were already published in article *Influence of nitrogen species on the porous-alumina-assisted growth of TiO_2 nanocolumn arrays (Bendova, Kolar, **Marik** et al).* where a crystallographic orientation of the nanocolumns with FFT was presented. The bottom of the roots, under the border of the Ti layer, reveals presence of nano-crystallites, however the rest of the nanocolumn had amorphous structure. (Figure 3.29.)

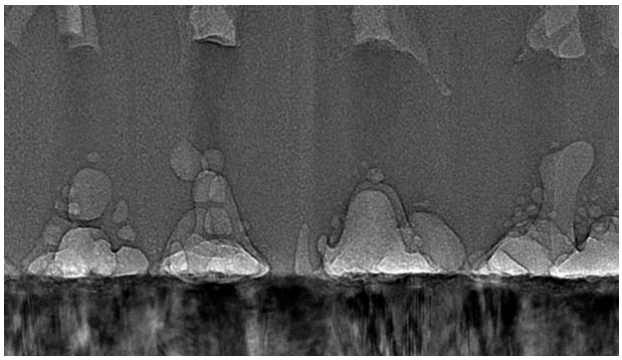

Figure 2.21.: HR-TEM image about the merged voids in the root system. The stems are transformed into one bell shaped root.

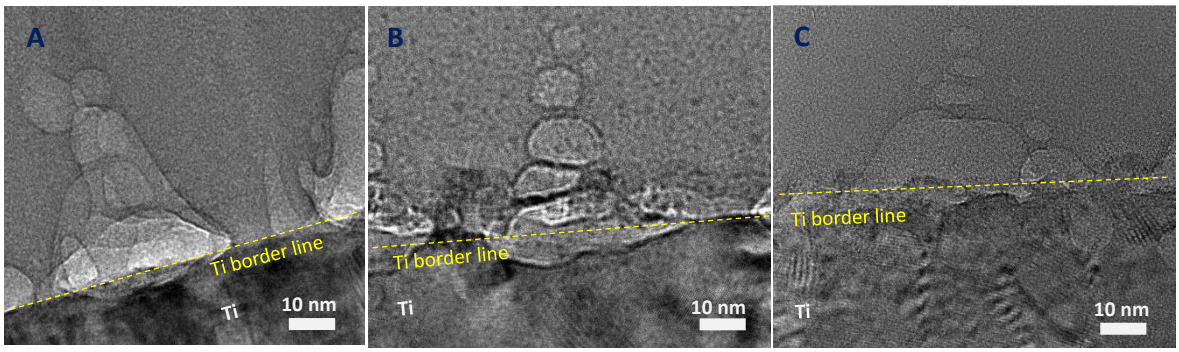

Figure 2.22.: HR-TEM images about the roots of re-anodized samples at 100V in as-anodized (A), vacuum annealed (B) and air annealed (C) conditions respectively. The crystalline structure of the Ti layer is visible with a nano-crystallites at the bottom of the roots under the Ti border line. The rest of the columns has amorphous structure.

The re-anodized samples were annealed in different conditions, therefore the oxygen distribution in the nanocolumns may change. The as-anodized sample considered as initial structure was observed by HR-TEM and EDX as well. Due to the low lamella thickness we can consider the observed nanocolumns were in one line and the scanned spectrum was not affected by other columns behind. EDX elemental maps of Al, Ti and O about the as-anodized samples were already published. Thin oxide layer at the bottom of the roots was compared with HR-TEM image, the thin oxide layer is under the Ti border line. This kind of disposition explains the above-mentioned nano- crystallites which are crystal residues from the Ti layer, mixed with amorphous TiO_2. The area of the oxide layer with nano-crystallites can be considered as an affected zone of anodic oxidation and the depth of the oxide under the Ti border line is considered as oxidizing depth. The oxidizing depth for as-anodized samples (re-anodized at 100V) is about 5 nm. Between the AAO and the Ti there is no affected zone and therefore the oxidizing depth for Al in Ti is 0nm. (Figure 2.23.)

Samples annealed in vacuum at 500°C for 2 hours and samples air annealed at 500°C for 2 hours respectively, were observed by TEM and EDX similarly to as-anodized samples. The heat-treated samples were re-anodized at 100V into a thin AAO, appropriate for sputtered Au top contacts. The initial Al layer after anodization reached a thickness which corresponded to a re-anodized TiO_2 column length. Before the lamella preparation a top Au contact was sputtered on the vacuum and air annealed samples, with a thickness about 200 nm. (Figure 2.24.)

The root system compared in Figure 2.22. showing a similar root structures with a few nanometers thin oxide mixture under the Ti border line. The top of the columns is different at annealed samples in comparison with as-anodized one. The as-anodized nanocolumns were re-anodized in a thick template, where the end of the columns has convex shaped top and they are located deeply in the AAO nano pores.

The annealed nanocolumns due to the thin AAO are branched or widened at the top of the template. The disposition of the pores at the beginning of the Al anodization forms some

thin pores which are merging in depth appx. 40-50 nm under the surface. This phenomenon leads to wider TiO_2 column tops.

The sputtered gold layer perfectly covers the nanocolumns, on the elemental maps there is no Au penetration into the TiO_2, however gold contaminants appeared on the side of the lamella at air annealed sample. This kind of contaminations are residues from lamella polishing.

The column length at both annealed parts are about 130 nm, measured from the Ti border line up to the top of the columns. The columns are affected by voids up to height 45-50 nm, measured from the bottom oxide under the borderline. Similarly, to the as-anodized sample, for the bottom oxide with nano-crystallites appx. 5 nm thickness was measured for both annealed samples, however the EDX elemental maps are shows for air annealed columns affected zone deeper than 5nm.

The samples were observed in STEM mode with bright field and dark field preset as well, where the differences between the vacuum annealed and air annealed affected zone were realized.

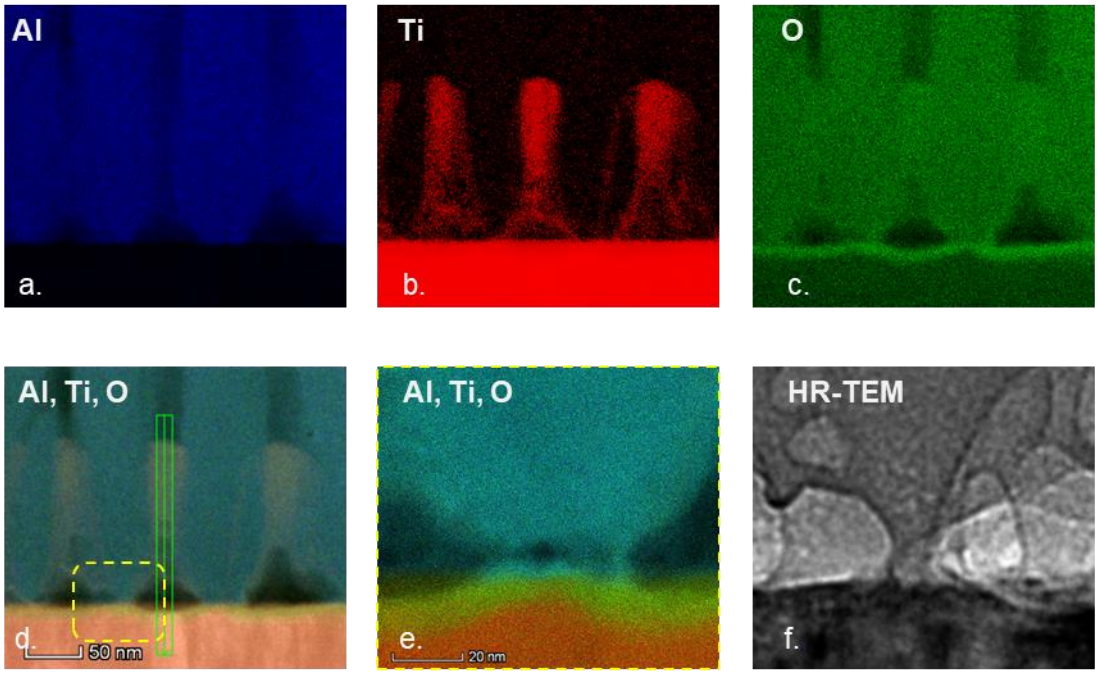

Figure 2.23.: Elemental maps from EDX analysis shown the distribution of the Al (a.), Ti (b.), O (c.) in the lamella from as-anodized sample. The position of the bottom oxide under the Ti border line is presented (d.), for better visibility magnified (e.). The nano-crystallite structure is visible on the HR-TEM image as well.

Under the air annealed roots in depth 10 to 20 nm a void zone was detected. The gap between the Ti border line and the void zone is crystalline Ti. This kind of inward oxygen migration during the anodization was not detected, respectively the vacuum annealed columns are consisting only bottom oxide with nano- crystallites.

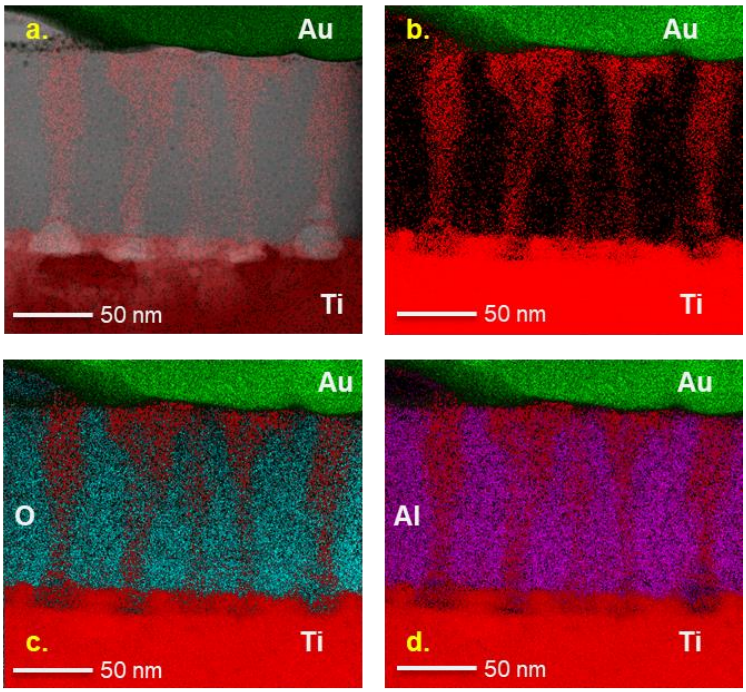

Figure 2.24.: Elemental maps about the nanocolumns after vacuum annealing. The STEM image fitted with elemental maps of Ti and gold shows the distribution of the Ti in the columns and the contact between the Au and the TiO_2 columns. (a.) Fitted maps without STEM image in combination of Ti – Au (b.), Ti-O-Au (c.), Ti-Al-Au (d.) are presented as well.

Responsible for such a deep oxygen migration can be only the air annealing. Air annealing is used for reduction of oxygen vacancies and during a heat treatment. At high temperature if the metal oxide is in reduced oxygen state it tends to balance the O_2 amount from the air. Through a saturated oxide the oxygen migration is possible in few cases. The nanocolumns prepared by anodic oxidation has amorphous structure with different oxygen proportion through the length of the column, moreover the roots are full of oxygen voids. The oxygen from the air penetrated through the amorphous columns and forced the O_2 voids under the bottom oxide layer. The distribution of the voids in the zone is not homogenous and their sizes are not steady as well. (Figure 2.25., Figure 2.26.)

The TiO_2, grown by anodic oxidation, obviously is a very good insulator. The vacuum annealed nanocolumns during the annealing were not crystallized, however the raise of their electrical conductivity was significant. The explanation for this phenomenon is the oxygen reduction in the columns which increases the amount of the oxygen vacancies.

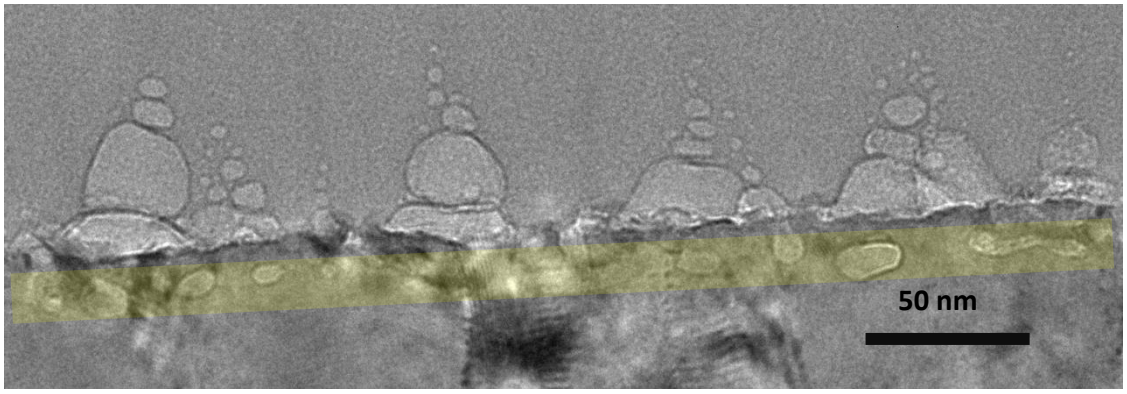

Figure 2.25.: Void zone under the air annealed columns is a unique and unexpected phenomenon found in depth 10 to 20 nm. The zone is highlighted with a transparent yellow band.

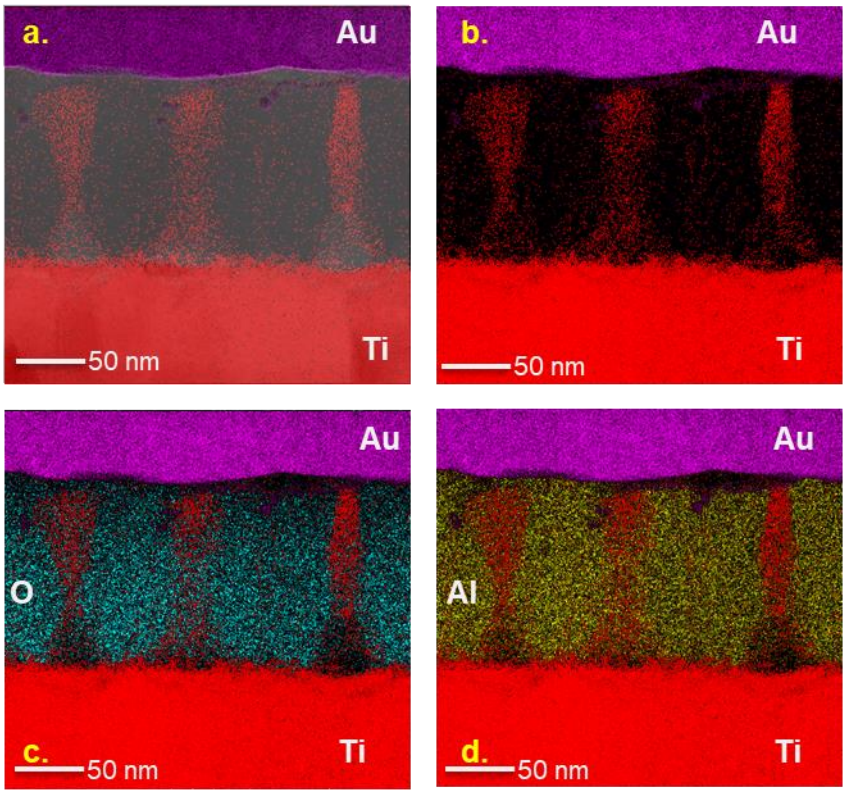

Figure 2.26.: Elemental maps about the nanocolumns after air annealing. The STEM image fitted with elemental maps of Ti and gold shows the distribution of the Ti in the columns and the contact between the Au and the TiO_2 columns. (a.) Fitted maps without STEM image in combination of Ti – Au (b.), Ti-O-Au (c.), Ti-Al-Au (d.) are presented as well.

2.8 Electrical Characterization

This chapter is dealing with electrical characterization of devices with TiO_2 nanocolumns. Every field of nanocolumns under one Au pad is considered as a two terminal electronic device. To identify the basic parameters and to get acquainted with the electrical behavior of the TiO_2 based MOM devices the current-voltage characteristics were measured and presented. The electrical characterization and the calculations of the Schottky barrier height are written below for some selected samples, however the characterization of the nanocolumns grown at sweep rate 2 $V \cdot s^{-1}$ is quoted literally from article *Resistive switching in TiO_2 nanocolumn arrays electrochemically grown (Marik et al)*. [*3.8.1 Quotation 1*]

The top electrodes were prepared with top down method, where the same photomask was used for every sample. To minimize the fails and the irrelevant results during the electrical characterization, the surface of the gold pads was measured with optical microscope. During the lithography and the chemical etching, the size of the top electrodes can be different, therefore the results are presented after recalculation of value of the electrical unit on a top electrode surface (as $A \cdot cm^{-2}$ or $\Omega \cdot cm^2$).

The initial cycle (the first cycle) usually can be considered as a forming cycle, especially if a current drop or jump is appeared. Initial cycle without current drop or jump was repeated on another device with higher potential up to 20V or up to reaching the current compliance level.

The potential for the consecutive cycling is always chosen based on the current jump/drop potential rounded up to a whole number in the forming curve.

2.8.1 Quotation 1.: Electrical characterization of nanocolumns electrochemically grown at sweep rate 2 V·s^{-1}.

The electrical characterization was performed at room temperature using a Keithley 4200 SMU system connected to a CASCADE M150 probe station with magnetic micromanipulators, by recording I(V) curves with a scan rate of 100 mV·s^{-1} from 0 to +5.0, then to −5.0 and back to 0 V in each cycle. To avoid damage of the microcells, the current compliance limit was set to 100 mA. The top Au pad was biased in all I(V) measurements, while the bottom Ti layer, remaining after the PAA-assisted anodizing and being common for all devices prepared on a single chip, was grounded. The measured current and the calculated resistance were related to the projected area of the microcells.

Typical initial I(V) characteristics of the arrays A (i.e. having the higher potential sweep rate during re-anodizing) processed to different final potentials are shown in figure 3a in a logarithmic representation to emphasize the differences between the samples. Each of these arrays, comprising TiO_2 nanocolumns of various lengths, reveals non-linear shape of the corresponding I(V) curve, also showing substantial current drops and jumps for the 70V and 130V arrays and an asymmetric diodelike behavior for the A-100V and A-130V samples. The initial resistance at 0 V (Rinitial,0V) increases with increasing re-anodizing potential, from ~0.25 Ω·cm^2 for sample A-70V to ~7.5 Ω·cm^2 for both A-100V and A-130V arrays. Further I(V) cycling (see figure 3b) shows again non-linear characteristics with an increased current density as compared with the initial state, being asymmetric only for the A-100V and A-130V arrays. The cycling resistance at 0 V (Rcycles,0V) is thus lower than that in the initial measurement by about ten and two times in case of sample A-70V and samples A100V and A-130V respectively

The electrical characterization of the arrays A therefore does not reveal any resistive switching behavior, for which a substantial decrease of resistance after the initial I(V) cycle accompanied by a presence of high- and low-resistance states (HRS and LRS, respectively) in the following cycles is expected. [57.] The observed current jumps and drops in the initial I(V) curves of arrays A (Figure 2.27. a.) are rather caused by imperfect contacting, and there are no signs of distinguishable HRS and LRS in the following cycles. On the other hand, the resistance increases with the re-anodizing potential, which is in line with the increasing length of the nanocolumns and with their semiconductive nature. In addition, as samples A-100V and A-130V have their initial and consecutive I(V)'s similar to each other but different from those of sample A-70V (see the curve shape and symmetry), different conduction mechanisms are expected in these array groups. The oxygen-deficient root structure [79.] of A-70V columns in the PAA barrier may prevail in the shorter nanocolumns, whereas a more stoichiometric, i.e. less conducting column body situated over the roots may lead to the diode-like behavior of A-100V and A-130V arrays, possibly with a Schottky barrier created at the Au/TiO_2 interface. [57.] To alter the electrical behavior of the PAA-assisted TiO_2 nanocolumns, an array of type B (i.e. having the lower potential sweep rate during re-anodizing) was also prepared and electrically characterized. An initial I(V) curve of sample B-100V (Figure 2.27. c.) shows a non-linear asymmetric behavior with $R_{initial,0V}$ of ~6·10^5

$\Omega \cdot cm^2$ and a current jump at 5.0 V, leading to a drop in the resistance of about one order of magnitude. The consecutive cycling (Figure 2.27. d.) reveals also a non-linear asymmetric I(V) characteristic and, in addition, the presence of HRS and LRS having $R_{cycles,0V}$ of ~$3 \cdot 10^4$ and ~$8 \cdot 10^3$ $\Omega \cdot cm^2$, respectively. The array B-100V shows therefore signs of bipolar resistive switching. During the initial, forming I(V) cycle, a conducting filament is probably formed within the columns or at one of the interfaces. [57.]

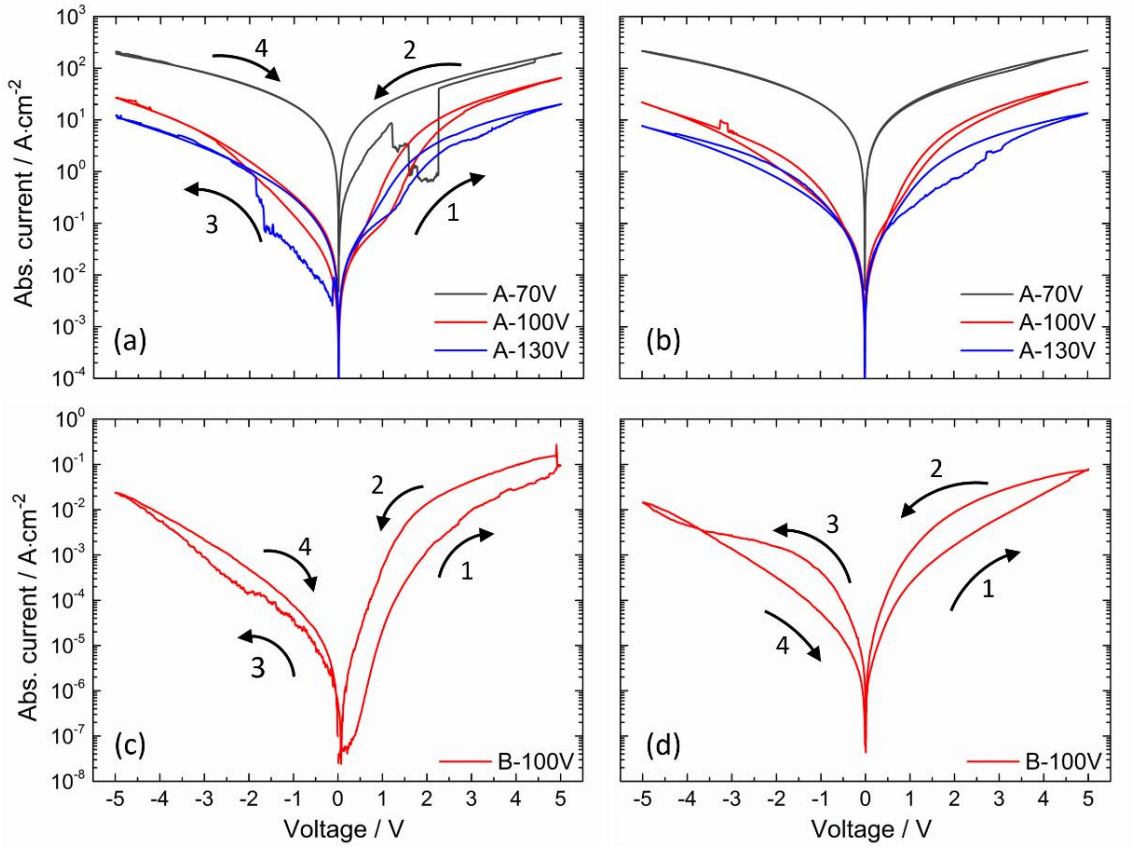

Figure 2.27.:(a, c) The initial and (b,d) further *I*(*V*) cycles obtained (a, b) for arrays A (i.e. formed at the higher potential sweep rate during re-anodizing) and (c, d) for arrays B (i.e. formed at the lower potential sweep rate during re-anodizing). The cycling was performed in the order 0 → +5.0 → −5.0 → 0 V without any break in applying voltage, at a scan rate of 100 $mV \cdot s^{-1}$ at room temperature. The top Au electrode was biased while the bottom Ti layer was grounded. The arrows indicate the scan direction

The switching direction, i.e. the transformation of HRS into LRS, happening at the positive polarization of the top Au electrode, followed by a transition from LRS into HRS at the negative polarization, indicates that the switching interface is the bottom one (TiO_2/Ti). [57.] The absence of abrupt current or resistance change during one of these transitions may indicate synaptic behavior of the array, [59.] executed in this case by inhomogeneous switching events in the multiple channels present in the array. Comparing the anodizing conditions during the nanocolumn growth with the electrical behavior of arrays A and B, we see the following relations, summarized schematically in Figure 2.28.. The higher potential sweep rate during the re-anodizing (arrays A) leads to the formation of nanocolumns having

a relatively low initial resistance (between 0.25 and 8 Ω·cm^2), whereas the lower potential sweep rate (array B) seems to increase the resistance (6·10^5 Ω·cm2). This may be explained by a formation of more oxygen-deficient and thus more electrically conducting nanocolumns in the case of the faster sweep rate during the column formation (arrays A) as compared to more stoichiometric oxide formed during the slower sweep rate (arrays B). [60.] Such higher-resistance, more-stoichiometric TiO_2 nanocolumns would be expected to lead to bipolar resistive switching behavior, [6.] as it is indeed observed in the present study. In addition, the length of the nanocolumns seems to have also an influence on their electrical resistance, possibly due to an inhomogeneous distribution of oxygen vacancies along the nanocolumn material, as manifested in arrays A by the increase in the resistance with increasing nanocolumn length, accompanied by the diode-like I(V) characteristics of the longer A-100V and A-130V nanocolumns. To confirm this mechanism, as well as to elucidate the role of the annealing in vacuum on the concentration and distribution of oxygen vacancies, further analytical and electrical characterization of the arrays is being performed. Additionally, TiO_2 nanocolumn arrays grown at modified electrochemical conditions are currently under investigation; the results to be reported in due course.

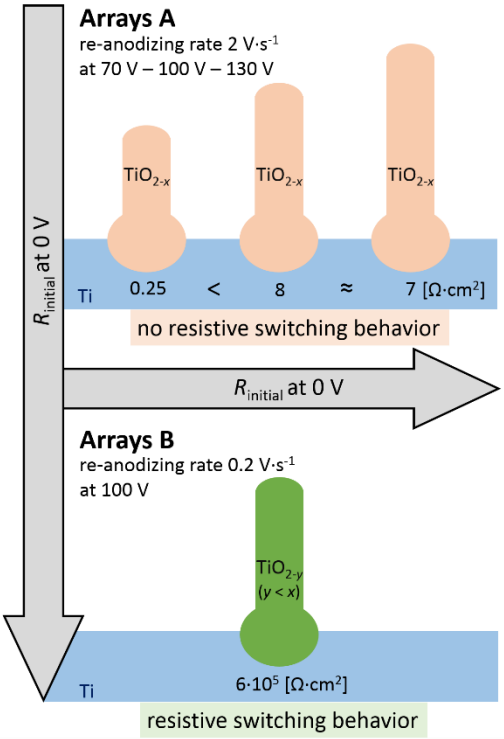

Figure 2.28.: Schematic representations of PAA-assisted-anodized TiO_2 nanocolumns re-anodized to different potentials showing the relations between the anodizing conditions, oxide stoichiometry, and electrical properties. The faster re-anodizing rate (arrays A, upper part) results in a lower $R_{initial,0V}$ and reveals no sign of resistive switching, whereas the slower re-anodizing rate (arrays B, lower part) leads to the formation of more stoichiometric columns having a high $R_{initial,0V}$ and showing the resistive switching.

End of the Quotation 1.

2.8.2 Electrical characterization of nanocolumns electrochemically grown at 40 V

Current-voltage curves for short nanocolumns anodized at 40V with electrodeposited gold top electrode and for long nanocolumns re-anodized at 100V with electrodeposited gold top electrode, above mentioned in the quotation as sample B-100V, were plotted. (Figure 2.29.) The values of the differential resistance were calculated, because the current and the voltage are not linearly proportional. The final resistance changes were presented as R_{dif} *(d V /d I)* – voltage curves.

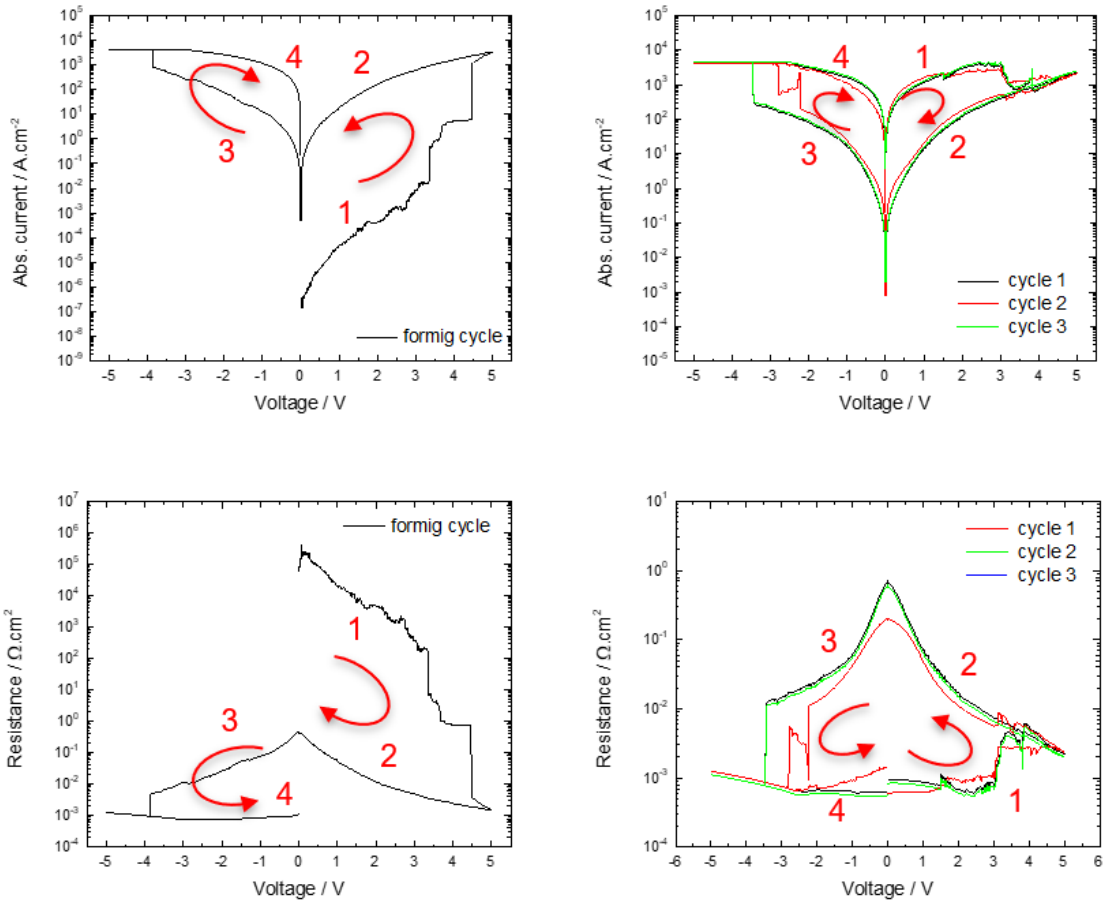

Figure 2.29.: Current - voltage and differential resistance - voltage curves from analyzed samples with columns anodized at 40V. The current and the resistance changes are marked and numbered for better understanding.

The initial I(V)curve similarly to the sample B-100V, quoted above, showing a non-linear asymmetric behavior with $R_{initial,0V}$ of ~$1{,}3 \cdot 10^5$ Ω·cm^2. The initial cycle can be considered as a forming cycle because a current jump at 4,5V leads to drop in the resistance of about two orders of magnitude. The resistance-voltage curves for short columns and for long columns (device B-100V) are presented and compared in Figure 2.30..

The consecutive cycling shows a non-linear and slightly asymmetric behavior, where at increased voltage at 3V a current drop increased resistivity from ~$1 \cdot 10^{-3}$ Ω·cm^2 to ~$8 \cdot 10^{-3}$ Ω·cm^2 and in-between -2,2V to -3,5V a current jump decreased resistivity approximately about one order of magnitude, form ~$1 \cdot 10^{-2}$ Ω·cm^2 to ~$1 \cdot 10^{-3}$ Ω·cm^2. The presence of HRS and LRS states during the cycling at 0V were observed with a resistance difference about two to three orders of magnitude. $R_{\_cycles,0V}$ were about ~$5 \cdot 10^{-1}$ Ω·cm^2 to ~$8 \cdot 10^{-4}$ Ω·cm^2.

The conductive filament during the initial cycle was formed. The transformation of LRS into HRS was observed at the positive polarization of the Au electrode and the transition from HRS to LRS at negative polarization. The switching interface probably is at the TiO_2/Au, nevertheless the realization process of the columns and the top electrode should be considered.

From previous material and structure evaluation the properties of the short nanocolumns were presented and the electrodeposition of the Au into the pores was written as well. Due to the small resistance values and the low potential at the current drops/jumps, the influence of the electrodeposition on the device is considered.

To avoid undesirable influences, the devices with re-anodized nanocolumns at 100V were prepared with sputtered Au top contacts in as anodized, air annealed and vacuum annealed conditions.

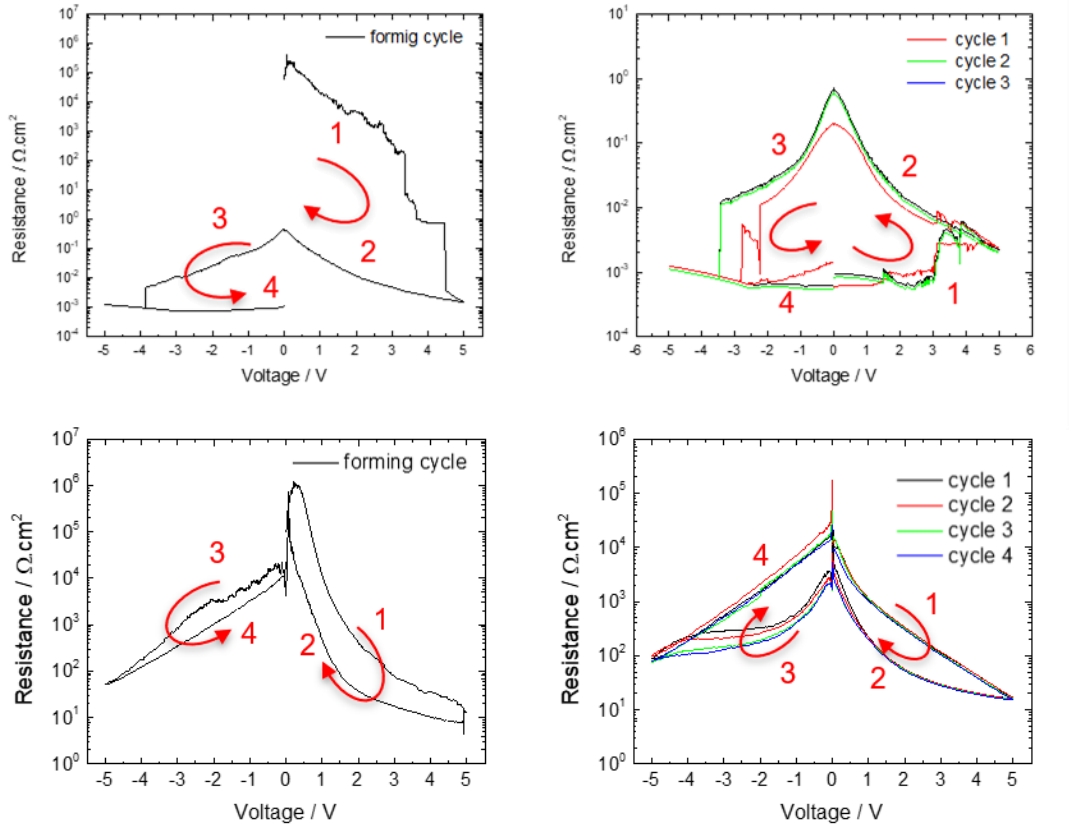

Figure 2.30.: LRS and HRS transition at devices with short and long nanocolumns. The switching direction is different, which suggests the switching interface is the TiO_2/Au for the short columns (a.) and Ti/TiO_2 is used at long columns. (b.)

2.8.3 Electrical properties of nanocolumns differently annealed

This chapter is dealing with electrical characterization of long nanocolumns, re-anodized at 100V into a thin AAO. The top of the columns reached the AAO surface, therefor the top Au contact was magnetron sputtered and shaped by lithography and wet etching respectively.

To ensure identic nanocolumns for all annealing set up, one anodized device was divided into four pieces. First quarter was left without annealing – device: A*s-Anodized*, the second quarter was annealed in vacuum at 500°C for 2 hours – device: *Vac500*, and the third quarter was annealed in air at 500°C for 2 hours – device: *Air500*. The fourth quarter was saved as a reserve piece. The top gold layer was prepared by magnetron sputtering on all three devices in a same time.

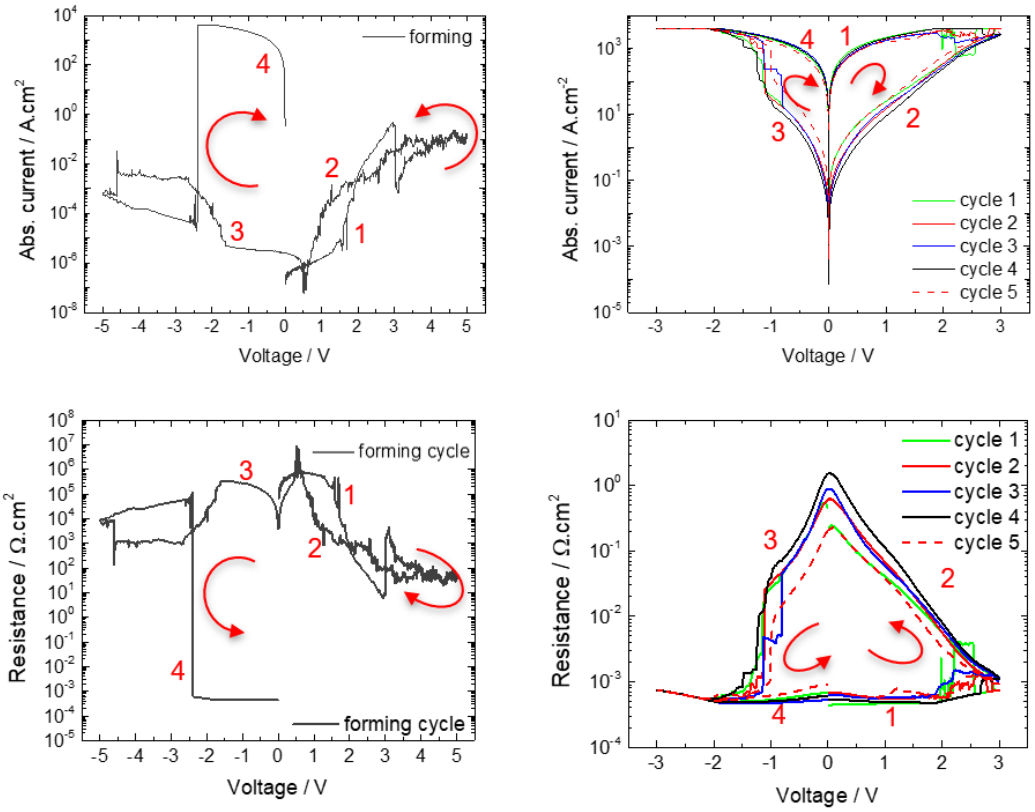

Figure 2.31.: LRS and HRS transition at AsAnodized device with long nanocolumns. The switching interface is probably the interface TiO_2/Au, similarly to the device with vacuum annealed short nanocolumns and electrodeposited top contact.

The initial I(V) curves were measured at room temperature (Rt) for all devices. As-anodized device was characterized at initial cycle ±5V, for the Vac500 and the Air500 ±10V was applied respectively. As-anodized sample shown interesting behavior at positively polarized top electrode, where increasing current from 1,7V to 3V was observed with a steep rising character from 1,7V to 2V and with linear rise from 2V to 3V, where a current drop about two orders of magnitude appeared. The current jump at negatively polarized Au electrode about 8 orders of magnitude at -2,5V reached current compliance level and the

high current was held between -2,5V to -1,7V, then the current decreased significantly. The same initial cycle set up was repeated on several As-anodized devices and similar current jump up to the current compliance level was observed between potentials about -2V to -4V.

The consecutive cycling potential range was set up for ±3 V, based on the potential levels of current drop/jump. (Figure 2.31 .) The device shown during the cycling nonlinear behavior, with a resistance difference at positively polarized top electrode about three orders of magnitude, $R_{\_cycles,0V}$ were about ~$7 \cdot 10^{-4}$ Ω·cm^2 to ~$6 \cdot 10^{-1}$ Ω·cm^2. At negatively polarized top electrode a current jump, about three orders of magnitude, was observed between -1,2 V to -1,5 V, that leads to RESET the device form HRS to LRS. Due to the transformation from LRS to HRS at positively polarized Au electrode, the switching interface is probably at the TiO_2/Au.

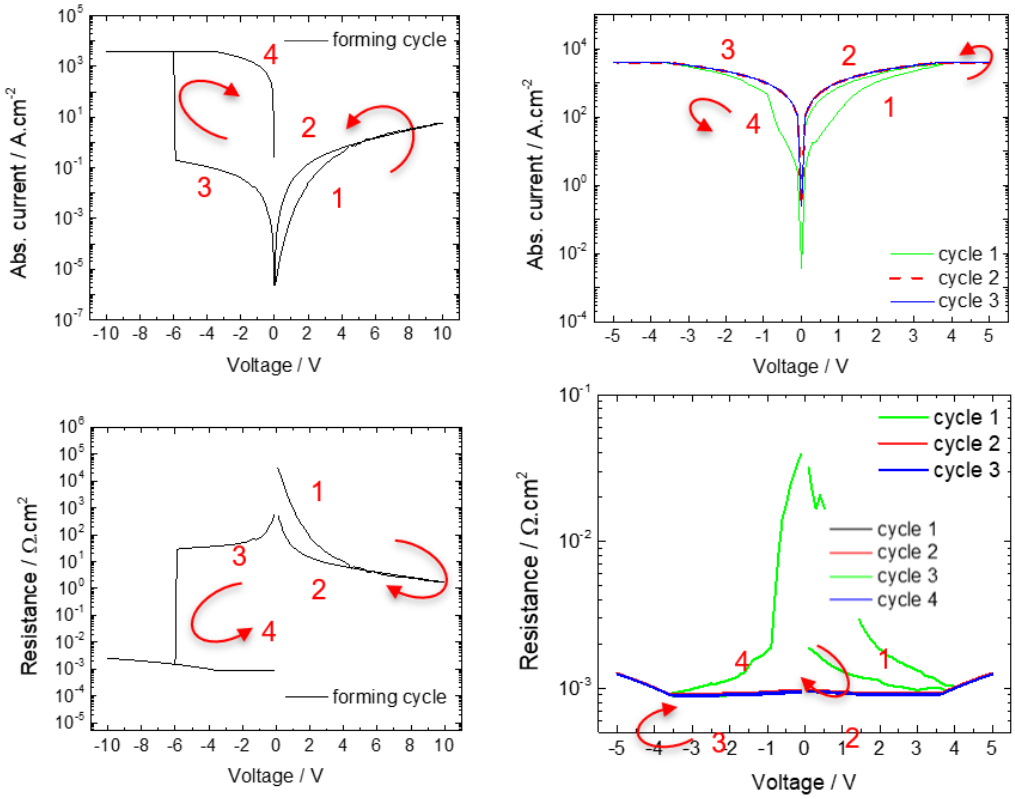

Figure 2.32.: Electrical characterization of vacuum annealed device. The forming cycle with current direction is comparable with AsAnodized sample. The consecutive cycling from the 2nd cycle shown symmetric diode like character, without HRS and LRS switching tendency.

Device Vac500 was characterized at three different cycling potentials, at ±5V, ±10V, ±20V. Attempts to find a proper potential range for formation of the device were unsuccessful at ±5V and at ±20V as well. The initial cycle at ±5V shown a diode like behavior at positive and negative top contact polarization. The device at potential range ±20V shown a diode like behavior at positively polarized top contact, however at negative polarization a current jump at -6 V was observed. The current jump about four orders of magnitude

reached the current compliance level and the device did not shown any switching behavior at consecutive cycling. Similar results were achieved at ±10V cycling set up, where at -6V at negatively polarized top contact a current jump about four orders of magnitude reached the current compliance level. Due to above mentioned results from initial cycling at different ranges a consecutive cycle range was declared as ±5V. The device shown symmetric diode like behavior from the 2nd cycle at positive and negative polarization of the Au contact. At cycle 1 a small difference about one order of magnitude, $R_{\_cycle1\_0V}$ were about ~$1 \cdot 10^{-2}$ Ω·cm^2 to ~$2{,}8 \cdot 10^{-1}$ Ω·cm^2.

The symmetric diode like character of the device is probably caused by a Schottky barrier on TiO_2/Au interface at positively polarized Au. The Ti/TiO_2 interface behaves as an ohmic contact in this case. Calculating of Schottky barrier height, if there is any Schottky contact available on Ti/TiO_2 interface, can help to understand electrical behavior of this device.

Air annealed device was characterized at potential ranges ±5V, ±10V and ±20V. The current compliance level was reached from 19,6V to 20V and then the device shown only non-linear diode like character for both polarizations of the top electrode. The initial I(V) curve after cycling at potential ±10V shown asymmetric non-linear character with a steep current rise from $I_{\_initial\_7,6V}$ = ~$6{,}5 \cdot 10^{-5}$ A·cm^{-2} to $I_{\_initial\_8,3V}$ = ~$4{,}3 \cdot 10^{-4}$ A·cm^{-2} and then with a moderately steep rising a current level $I_{\_initial\_10V}$ = ~$5 \cdot 10^{-3}$ A·cm^{-2} was observed. With decreasing potential, a steep current rising was observed from 0,5 V to 0 V. Similar current behavior was observed at negatively polarized top electrode from potential -3,1 V to 0 V, where the current level increased about one order of magnitude. (Figure 2.33.)

The consecutive cycling shown current level difference at positively polarized top contact at 9V about 2 orders of magnitude. The current decreased in almost linear way between potential 8 V to 1 V. From 1 V to 0 V the current drop and jump was observed, and similar current behavior appeared at negatively polarized gold contact between ranges -5,5 V to -4,5 V and -2 to -1 V.

If the above-mentioned current behavior at the positive and at the negative Au polarization is appearing, probably a capacitive coupled diode like behavior was measured, [68.] Moreover, the non-zero crossing current voltage behavior also proofs the presence of the capacitive state in the device.

The presence of HRS and LRS states during the cycling was not observed, however at 0V a resistance $R_{\_cycles,0V}$ about ~$4{,}3 \cdot 10^{-5}$ Ω·cm^2 to ~$9{,}6 \cdot 10^{-5}$ Ω·cm^2 was measured.

The electrical behavior of the Air500 device can be caused by more stoichiometric TiO_2 and the oxygen distribution through the roots and the column. Furthermore, the device behaves as a linear resistor between 8V to 1 V, where the current decreased in a linear way.

The electrical characteristic of the device Air500 at positively polarized top contact suggests the existence of a Schottky interface barrier at the TiO_2/Au.

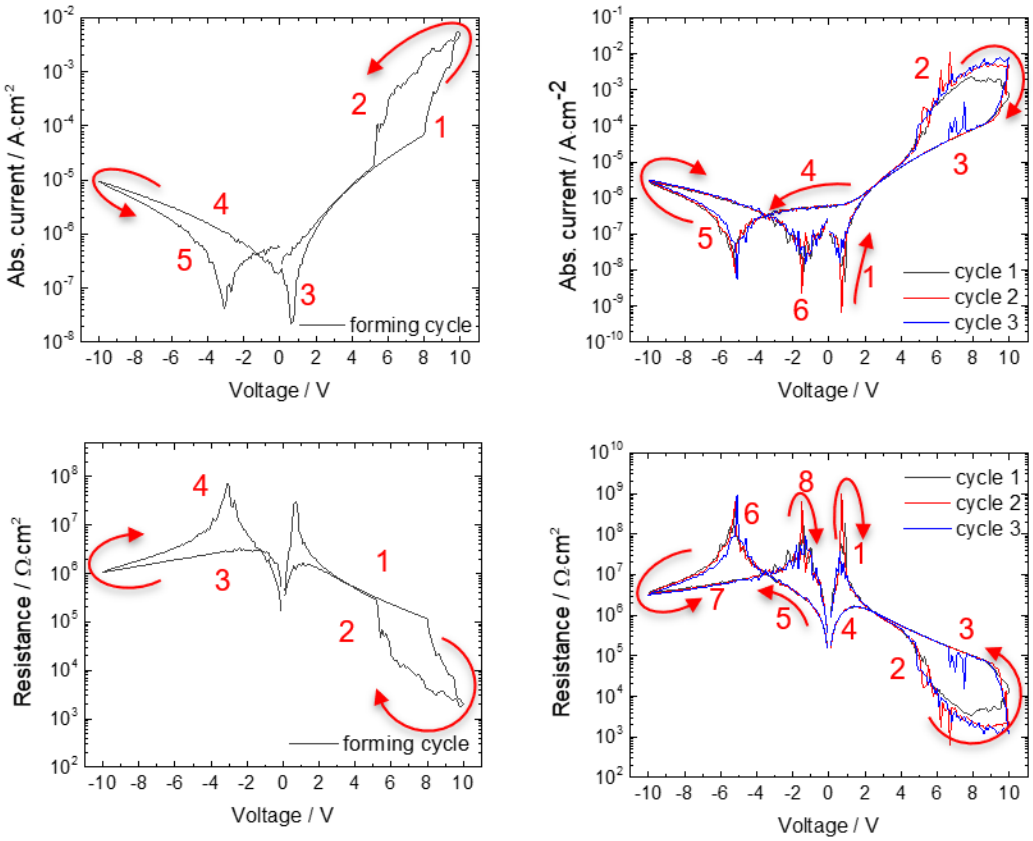

Figure 2.33.: Electrical characteriyation of air annealed device Air500. The current behavior during the cycling is suggest to a capacitive coupled diode behavior.

The measured I(V) characteristics were compared with characteristics from other *transient metal/transient metal oxide/noble metal* devices [57.][80.] where similar non/linear characters were observed. The asymmetric current voltage behaviors are probably caused by a formation of a rectifying Schottky junction on oxide/metal interfaces in case of as-anodized devices and air annealed devices respectively.

At positive polarization of the top electrode (Au) the only limiting electron transport feature is the Schottky-like barrier formed at TiO_2 interface. The Ti/TiO_2 interface is considered as an ohmic contact. This is consistent with the work function and electron affinities of the materials involved (for Au: 5,4 eV [61.], for Ti: ~4,1-4,3 eV [61.] and for TiO_2: ~4,4-5 eV [61.]).

In the nanocolumns the concentration of the oxygen vacancies are acting as electron donors, which concentration at the top of the columns is depending on the annealing set up or the Schottky barrier is higher due to the thicker depletion layer at the TiO_2/Au interface. This phenomenon was observed at other anodized transition metals as well. [57.] The ohmic or non-rectifying contact at the Ti/TiO_2 interface was written by *Michalas et. al.*.

Asymmetric I(V) characteristics are typical for interface-controlled transport, which can be dominated by a thermionic emission or by tunneling through the formed barrier at the interface. These two types of transport are easily distinguishable via temperature dependence of the I(V) characteristics furthermore for interface-controlled transport the most common thermally activated mechanism is the thermionic emission. [81.]

Temperature dependent I(V) curves were plotted as logI vs. logV and logI vs. $V^{1/2}$ for positively and negatively polarized top electrode (Figure 2.34., Figure 2.35.). The saturation current I_0 was evaluated from semi-logarithmic plots of the temperature dependent I(V) curves. These above written curves were obligatory to calculate Schottky barrier height.

The current in reverse direction can be calculated by equation

$$I_R = A^* \times T^2 \times e^{\frac{-q\left(\Phi_B - \sqrt{\frac{q}{4\varepsilon\pi d}} \times \sqrt{V_R}\right)}{kT}}, \quad (21)$$

where I_R is the reverse current density, A* is the effective Richardson constant, Φ_B is the Schottky barrier height, ε is the permittivity of TiO_2, and d is the depletion layer. Based on this equation the *log*I ($V^{1/2}$) plots have linear dependence in ideal case. [57.][61.][62.]

For As-Anodized device the plots hardly can be called as a linear, however the current density is in a range of one order of magnitude for all temperatures. Based on this behavior the temperature dependency at As-Anodized sample is questionable at low potential.

Vac500 device shown linear tendency in reverse direction in plots *log*I ($V^{1/2}$), with increasing current density at higher temperatures. However, two ranges were observed, from Rt to 140°C and from 180°C to 230°C, where the current density of the curves in range from 180°C to 230°C were lower than at 65°C.

Air500 device shown linear tendency in reverse direction in plots *log*I ($V^{1/2}$), with increasing current density at higher temperatures.

The equation (21) rewritten into form:

$$ln\frac{I_R}{T^2} = lnA^* - \frac{1}{T} \times \frac{q}{k}\left(\Phi_B - \sqrt{\frac{q}{4\varepsilon\pi d}} \times \sqrt{V_R}\right), \quad (22)$$

With plotted Richardson plots *lnI/T²(1/T)* for all three devices and with method from Bendova et al. the constant value of *lnA** independent on the reverse potential is defined, the values of the Schottky barrier height Φ_B and the depletion layer depth *d* was calculated respectively.[57.]

The currents in forward direction can be written as

$$ln\frac{I_F}{T^2} = lnA^* - \frac{1}{T} \times \frac{q}{k}(\Phi_B - V_F), \quad (23)$$

and they were plotted as Richardson plots, *lnI/T²(1/T)* for all three devices. ([57.] and with above used method the value of *lnA**, the Schottky barrier height Φ_B and the depletion layer depth *d* was calculated. The results are summarized in Table 5. [57.][61.]

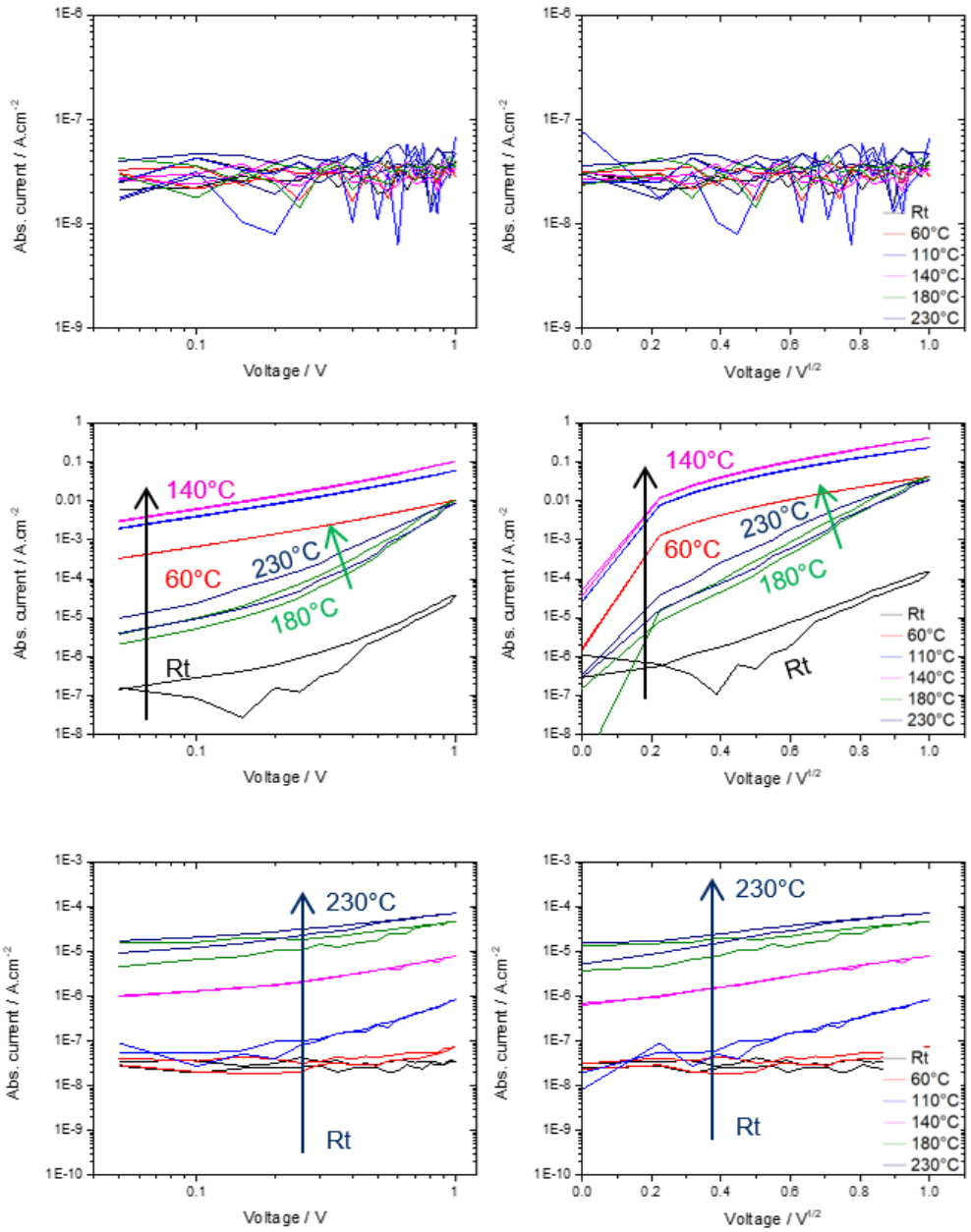

Figure 2.34.: Temperature dependent I(V) curves were plotted as logI vs. logV

and logI vs. $V^{1/2}$ for positively polarized top electrode

The Schottky barrier height Φ_B was calculated from the saturation current density I_0, which was earned by extrapolation of the current density at 0V red from the semi-logarithmic plots in forward direction, presented in Figure 3.43.

The Φ_B was calculated as

$$\Phi_B = \frac{kT}{q} ln \frac{A^* T^2}{I_0} \quad (24)$$

[57.][61.] and compared with values from previous calcualtions in Table 5.

The temperature dependent current voltage curves were plotted for positive and negatative polarization of Au electrode and the Schottky junction presence at the Ti/TiO_2

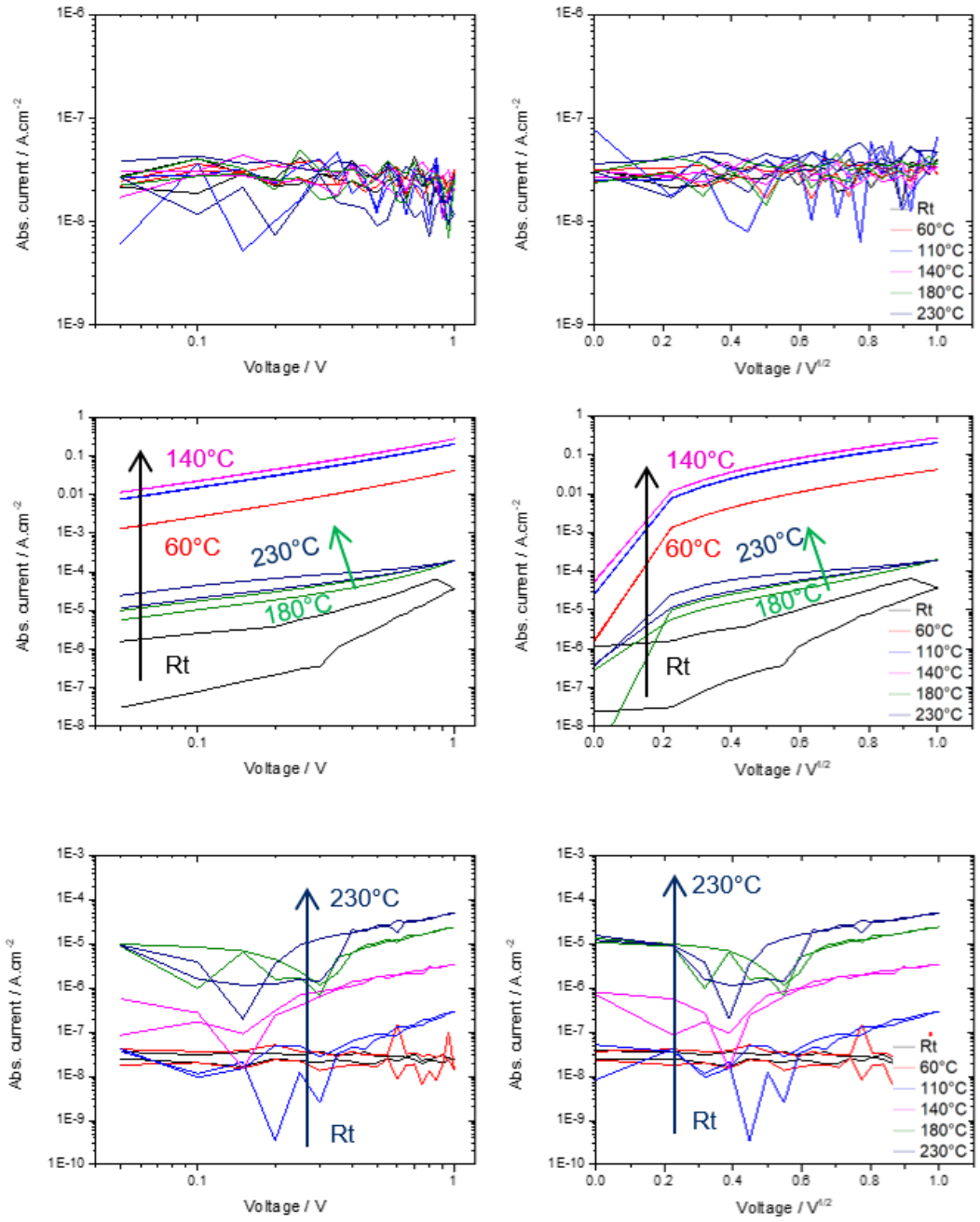

Figure 2.35.: Temperature dependent I(V) curves were plotted as logI vs. logV and logI vs. $V^{1/2}$ for positively and negatively polarized top electrode

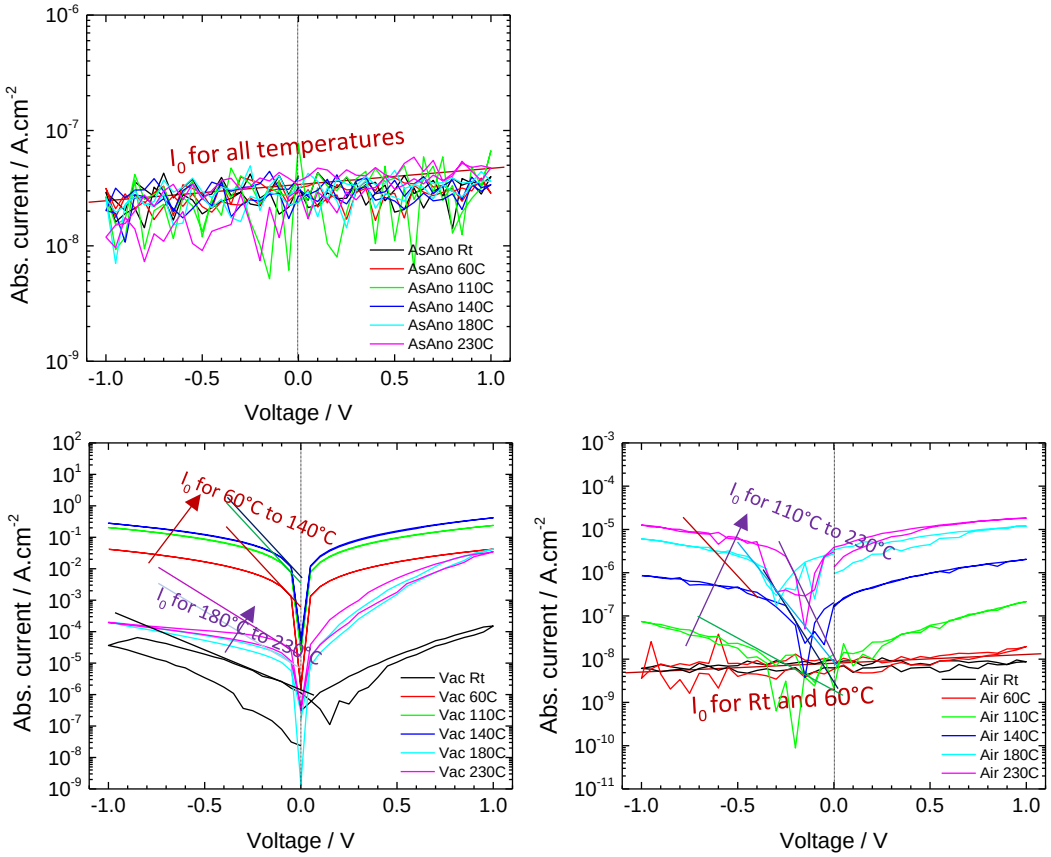

Figure 3.36.: Extrapolated current density in forward direction at as anodized, vacuum annealed and air annealed devices. The current density I_0 was red from the curves manually, therefore small inaccuracy in the results may appear.

Table 2.: Summarized Schottky barrier heights for as anodized, vakuum annealed and air annealed devices, respectively.

	Forward dierction (neg. top electrode)		**Reverse direction (pos. top electrode)**		**Forward direction I0 method**	**Reverse direction I0 method**
	ΦB [eV]	***d [nm]***	***ΦB [eV]***	***d [nm]***	***ΦB [eV]***	***ΦB [eV]***
As anodized	1,11	0,68	0,54	0,6	0,56	0,3
Vacuum annealed	-0,43	1,6	-4,91	3,3	-0,2	-0,32
Air annealed	-1,84	2,9	-4,72	2,4	-0,21	-0,4

Schottky barrier heights and depletion layer thicknesses summarized in Table 5. are corresponding with the first conclusions from the IV characterizations. The as-anodizded

device with a Schottky barrier height at BE and the nanocolumns are lower, than at the TE. The resistive switching at this device is real, the switching interface is between the oxide layer and the TE.

The vacuum annealed and the air annealed devices shown diode like behavior, which was confirmed by the calculations of the Schottky barrier height. The calculations were given negative values for Schottky barrier height at vacuum annealed and air annealed device, respectively. This rare phenomenon at the Ti/TiO_2 interface can be presented as an ohmic contact. Similar phenomenon at different material combinations was observed and published by [82.]

The calculations of Schottky barrier heights with I_0 method brought similar results as above written calculations. The device with as-anodized nancolumns shown Φ_B 0,56 eV (prev. calc. 1,11 eV) in forward direction and 0,3 eV (prev. calc. 0,54 eV) in reverse direction. The difference between the calculated SBH are negligible and they can be considered as realistic resuls.

The SBH for the vacuum annealed and air annealed devices are in negative range with both calculation methods. The tenfold difference between the values in reverse direction was probably caused by the differences between the calculation methods. The lower SBH with I_0 method can be closer to the reality.

3 CONCLUSION

Resistive switching in MOM devices is an actual topic with huge possibilities in many fields, as computer sciences, systems with artificial intelligence, analogue and digital electronics, etc.

In this work, the prepared nanostructures were analyzed from material and structural view with several high-tech techniques.

Fabrication of the highly self-ordered nanocolumn arrays in AAO template with different root structures, opened new possibilities and showed possible challenges from realization to characterization as well. The short nanocolumns with a void-full tooth like root structure are helped to understand their growing process, the differences between the voltage sweep rates on the root structures were also visible on the root structures.

Effect of the annealing properties were presented by three device groups - as anodized, vacuum annealed and air annealed devices, where the self-ordered AAO with the TiO_2 nanocolumns were prepared in identic way, only the annealing step was different. The nanocolumns remained amorphous in all three cases, however at the bottom of the roots under the Ti borderline a thin layer of nano-crystallites was detected.

The electrical characterization of the devices was provided on Keithley 4200 SMU, where a resistive switching behavior was detected at short (anodized at 40V) vacuum annealed device with electrochemically deposited gold TE and at as anodized device with magnetron sputtered gold TE, respectively. The device with short vacuum annealed columns had low endurance, therefore it was not included to the experiments dealing with the Schottky barrier height declaration.

The SBH at the Ti/TiO_2 interface was calculated with two methods for all three differently annealed devices. The as anodized device with resistive switching properties had SBH between 1,11 eV (forward direction) and 0,54 eV (reverse direction). The shigher SBH at interface TiO_2/Au and the switching direction from LRS to HRS suggests, the switching interface is between the column and the TE. The vacuum and air annealed devices shown only diode like behavior with negative SBH at the BE and column interface, what is considered as an ohmic contact.

The length of the nanocolumns requires higher potential (few volts) to show any resistive switching or diode like behavior, therefore their future area of use can be mainly in analogue techniques where a capacitive coupled diode circuits are required or at slower digital techniques where higher potentials (few Volts) can be used for writing and lower potentials for reading.

Table 6.: Overview about the results of the electrical characterization of three devices, differently annealed.

Anodizing potential	Sweep rate for re-anodization	Sweep rate for re-anodization	Annealing set up		
	0,2 $V \cdot s^{-1}$	2 $V \cdot s^{-1}$	As-Anodized	500°C/2h in Vacuum	500°C/2h in Air
40V	Resistive switching appeared: LRS to HRS difference is about 3 orders of magnitude. Switching interface: oxide/TE.	No sweep rate differencies at 40V.	Difficulties during gold sputtering into the AAO. The pores were too narrow and too long for magnetron sputtering.	Difficulties during gold sputtering into the AAO. The pores were too narrow and too long for magnetron sputtering.	Difficulties during gold sputtering into the AAO. The pores were too narrow and too long for magnetron sputtering.
40V re-anodized at 100V	Resistive switching appeared: LRS to HRS difference is about 3 orders of magnitude. Switching interface: oxide/TE. SBH was not calculated due to different TE deposition technique.	No RS behavior, only diode like behavior was measured. The resistance of the columns are increasing with the length.	Resistive switching appeared: LRS to HRS difference is about 3 orders of magnitude. Switching interface: oxide/TE. SBH at BE/oxide is about 1,11 to 0,54 eV.	No RS behavior, only diode like behavior was measured. The active interface is at the oxide/TE. The SBH at the BE/oxide is about -0,2 to -4,9 eV.	No RS behavior, only capacitive coupled diode like behavior was detected. The active interface is at the oxide/TE. The SBH at the BE/oxide is about -0,2 to -4,7 eV. The capacitive character is probably caused by the void zone in the BE.
40V re-anodized at 130V	Device damage during re-anodization.	No RS behavior, only diode like behavior was measured. The resistance of the columns are increasing with the length.	Device damage during re-anodization.	Device damage during re-anodization.	Device damage during re-anodization.

4 REFERENCES

[1.] Schaller, R. R. Moore's law: past, present and future. IEEE Spectr. 34, 52–59 (1997).

[2.] TETZLAFF, RONALD, Memristors and memristive systems. 403, 2014, ISBN 978-1-4614-9068-5.

[3.] Strukov, D. B., Snider, G. S., Stewart, D. R. & Williams, R. S. The missing memristor found. Nature 453, 80–83 (2008).

[4.] Krestinskaya, O., Irmanova, A. & James, A. P. Memristors: Properties, Models, Materials. in Modeling and Optimization in Science and Technologies 13–40 (Springer International Publishing, 2019). doi:10.1007/978-3-030-14524-8_2.

[5.] Chua, L. Memristor-The missing circuit element. IEEE Trans. Circuit Theory 18, 507–519 (1971).

[6.] Waser, R., Dittmann, R., Staikov, G. & Szot, K. Redox-Based Resistive Switching Memories - Nanoionic Mechanisms, Prospects, and Challenges. Adv. Mater. 21, 2632–2663 (2009).

[7.] Jeong, D. S. et al. Emerging memories: resistive switching mechanisms and current status. Rep. Prog. Phys. 75, 076502 (2012).

[8.] NISHI, YOSHIO, Advances in non-volatile memory and storage technology. Elsevier, 2014, 532. ISBN 9780857098030.

[9.] Kim, S., Choi, S., Lee, J. & Lu, W. D. Tuning Resistive Switching Characteristics of Tantalum Oxide Memristors through Si Doping. ACS Nano 8, 10262–10269 (2014).

[10.] Braganca, P. M. et al. A Three-Terminal Approach to Developing Spin-Torque Written Magnetic Random Access Memory Cells. IEEE Trans. Nanotechnology 8, 190–195 (2009).

[11.] Kim, S., Jeong, H. Y., Kim, S. K., Choi, S.-Y. & Lee, K. J. Flexible Memristive Memory Array on Plastic Substrates. Nano Lett. 11, 5438–5442 (2011).

[12.] Li, Y. et al. An overview of resistive random access memory devices. Chin. Sci. Bull. 56, 3072–3078 (2011).

[13.] Lacaita, A. L. & Redaelli, A. The race of phase change memories to nanoscale storage and applications. Microelectronic Engineering 109, 351–356 (2013).

[14.] Burr, G. W. et al. Phase change memory technology. Journal of Vacuum Science & Technology B, Nanotechnology and Microelectronics: Materials, Processing, Measurement, and Phenomena 28, 223–262 (2010).

[15.] Sawa, A. Resistive switching in transition metal oxides. Materials Today 11, 28–36 (2008).

[16.] Endres, F. et al. On the electrodeposition of titanium in ionic liquids. Phys. Chem. Chem. Phys. 10, 2189 (2008).

[17.] Mozalev, A., Gorokh, G., Sakairi, M. & Takahashi, H. The growth and electrical transport properties of self-organized metal/oxide nanostructures formed by anodizing Ta-Al thin-film bilayers. J Mater Sci 40, 6399–6407 (2005).

[18.] Chua, L. O. & Sung Mo Kang. Memristive devices and systems. Proc. IEEE 64, 209–223 (1976).

[19.] Sun, J. Z. et al. A three-terminal spin-torque-driven magnetic switch. Appl. Phys. Lett. 95, 083506 (2009).

[20.] Efeoglu, H., Güllülü, S. & Karacali, T. Resistive switching of reactive sputtered TiO_2 based memristor in crossbar geometry. Applied Surface Science 350, 10–13 (2015)

[21.] Waser, R., Dittmann, R., Staikov, G. & Szot, K. Redox-Based Resistive Switching Memories - Nanoionic Mechanisms, Prospects, and Challenges. Adv. Mater. 21, 2632–2663 (2009).
[22.] Ye, C. et al. Physical Mechanism and Performance Factors of Metal Oxide Based Resistive Switching Memory: A Review. Journal of Materials Science & Technology 32, 1–11 (2016).
[23.] Lee, J. S., Lee, S. & Noh, T. W. Resistive switching phenomena: A review of statistical physics approaches. Appl. Phys. Rev. 2, 031303 (2015).
[24.] Kröger, F. A. & Vink, H. J. Relations between the concentrations of imperfections in solids. Journal of Physics and Chemistry of Solids 5, 208–223 (1958).
[25.] Strukov, D. B., Alibart, F. & Stanley Williams, R. Thermophoresis/diffusion as a plausible mechanism for unipolar resistive switching in metal–oxide–metal memristors. Appl. Phys. A 107, 509–518 (2012).
[26.] Zhou, G. D. et al. Mechanism for bipolar resistive switching memory behaviors of a self-assembled three-dimensional MoS2 microsphere composed active layer. Journal of Applied Physics 121, 155302 (2017).
[27.] Rozenberg, M. J. et al. Mechanism for bipolar resistive switching in transition-metal oxides. Phys. Rev. B 81, (2010).
[28.] Pickett, M. D. et al. Switching dynamics in titanium dioxide memristive devices. Journal of Applied Physics 106, 074508 (2009).
[29.] Ielmini, D. Resistive switching memories based on metal oxides: mechanisms, reliability and scaling. Semicond. Sci. Technol. 31, 063002 (2016).
[30.] Miller, K., Nalwa, K. S., Bergerud, A., Neihart, N. M. & Chaudhary, S. Memristive Behavior in Thin Anodic Titania. IEEE Electron Device Lett. 31, 737–739 (2010).
[31.] Michaelis, A. Valve Metal, Si and Ceramic Oxides as Dielectric Films for Passive and Active Electronic Devices. Advances in Electrochemical Sciences and Engineering 1–106 (2008) doi:10.1002/9783527625307.ch1.
[32.] Mozalev, A., Magaino, S. & Imai, H. The formation of nanoporous membranes from anodically oxidized aluminium and their application to Li rechargeable batteries. Electrochimica Acta 46, 2825–2834 (2001).
[33.] Mozalev, A., Surganov, A. & Magaino, S. Anodic process for forming nanostructured metal-oxide coatings for large-value precise microfilm resistor fabrication. Electrochimica Acta 44, 3891–3898 (1999).
[34.] Sjöström, T., Fox, N. & Su, B. Through-mask anodization of titania dot- and pillar-like nanostructures on bulk Ti substrates using a nanoporous anodic alumina mask. Nanotechnology 20, 135305 (2009).
[35.] Sjöström, T., Fox, N. & Su, B. A study on the formation of titania nanopillars during porous anodic alumina through-mask anodization of Ti substrates. Electrochimica Acta 56, 203–210 (2010).
[36.] Zukalova, M., Bousa, M., Bastl, Z., Jirka, I. & Kavan, L. Electrochemical Doping of Compact TiO_2 Thin Layers. J. Phys. Chem. C 118, 25970–25977 (2014).
[37.] KOLAR, Jakub. Studium odporového spínání v paměťových celách na bázi iontově vodivých chalkogenidů a nanoporézního oxidu hlinitého [online]. Pardubice, 2013, Dissertation work. University Of Pardubice, Faculty Of Chemical Technology Department Of General And Inorganic Chemistry
[38.] Yang, J. J., Strukov, D. B. & Stewart, D. R. Memristive devices for computing. Nature Nanotech 8, 13–24 (2012).

[39.] Tatarenko, N. I. & Mozalev, A. M. Geometry and element composition of a nanoscale field emission array formed by self-organization in porous anodic aluminum oxide. Solid-State Electronics 45, 1009–1016 (2001).
[40.] Kao, T.-T. & Chang, Y.-C. Influence of anodization parameters on the volume expansion of anodic aluminum oxide formed in mixed solution of phosphoric and oxalic acids. Applied Surface Science 288, 654–659 (2014).
[41.] Yang, J. J. et al. Memristive switching mechanism for metal/oxide/metal nanodevices. Nature Nanotech 3, 429–433 (2008).
[42.] Bendova, M., Kolar, J., Marik, M., Lednicky, T. & Mozalev, A. Influence of nitrogen species on the porous-alumina-assisted growth of TiO_2 nanocolumn arrays. Electrochimica Acta 281, 796–809 (2018).
[43.] Marik, M., Mozalev, A., Hubalek, J. & Bendova, M. Resistive switching in TiO_2 nanocolumn arrays electrochemically grown. J. Phys.: Conf. Ser. 829, 012001 (2017).
[44.] Kwon, D.-H. et al. Atomic structure of conducting nanofilaments in TiO_2 resistive switching memory. Nature Nanotech 5, 148–153 (2010).
[45.] .Lamberti, A. et al. Ultrafast Room-Temperature Crystallization of TiO_2 Nanotubes Exploiting Water-Vapor Treatment. Sci Rep 5, (2015).
[46.] Merrikh Bayat, F., Hoskins, B. & Strukov, D. B. Phenomenological modeling of memristive devices. Appl. Phys. A 118, 779–786 (2015).
[47.] Lee, W. & Park, S.-J. Porous Anodic Aluminum Oxide: Anodization and Templated Synthesis of Functional Nanostructures. Chem. Rev. 114, 7487–7556 (2014).
[48.] Marchewka, A. et al. Nanoionic Resistive Switching Memories: On the Physical Nature of the Dynamic Reset Process. Adv. Electron. Mater. 2, 1500233 (2015)
[49.] Vázquez, R. M. et al. The Growth and Gas Sensing Properties of Mixed Oxide Nanocomposite Thin Film Derived from Anodically Oxidized Al/Ti Metal Layers. Procedia Engineering 47, 833–836 (2012).
[50.] Chen, X. & Mao, S. S. Titanium Dioxide Nanomaterials: Synthesis, Properties, Modifications, and Applications. Chem. Rev. 107, 2891–2959 (2007).
[51.] Macwan, D. P., Dave, P. N. & Chaturvedi, S. A review on nano- TiO_2 sol–gel type syntheses and its applications. J Mater Sci 46, 3669–3686 (2011).
[52.] Wu, J.-M., Shih, H. C. & Wu, W.-T. Electron field emission from single crystalline TiO_2 nanowires prepared by thermal evaporation. Chemical Physics Letters 413, 490–494 (2005).
[53.] LIU, S. Straightforward fabrication of highly ordered TiO_2 nanowire arrays in AAM on aluminum substrate. Solar Energy Materials and Solar Cells (2004) doi:10.1016/j.solmat.2004.04.011.
[54.] Zhang, Y. et al. Titanate and titania nanostructured materials for environmental and energy applications: a review. RSC Adv. 5, 79479–79510 (2015).
[55.] Ge, M. et al. A review of one-dimensional TiO_2 nanostructured materials for environmental and energy applications. J. Mater. Chem. A 4, 6772–6801 (2016).
[56.] Mozalev, A. et al. Formation and gas-sensing properties of a porous-alumina-assisted 3-D niobium-oxide nanofilm. Sensors and Actuators B: Chemical 229, 587–598 (2016).
[57.] Bendova, M., Hubalek, J. & Mozalev, A. Exploring Electron Transport and Memristive Switching in Nanoscale Au/WO x /W Multijunctions Based on Anodically Oxidized Al/W Metal Layers. Adv. Mater. Interfaces 3, 1600512 (2016).
[58.] Zhang, T. et al. In situ growth of single-crystal TiO_2 nanorod arrays on Ti substrate: Controllable synthesis and photoelectro-chemical water splitting. Nano Res. 10, 1021–1032 (2017).

[59.] Chang, T. et al. Synaptic behaviors and modeling of a metal oxide memristive device. Appl. Phys. A 102, 857–863 (2011).
[60.] Knörnschild, G., Poznyak, A. A., Karoza, A. G. & Mozalev, A. Effect of the anodization conditions on the growth and volume expansion of porous alumina films in malonic acid electrolyte. Surface and Coatings Technology 275, 17–25 (2015).
[61.] Sze, S. M. & Ng, K. K. Physics of Semiconductor Devices. (John Wiley & Sons, Inc., 2006). doi:10.1002/0470068329.
[62.] Biju, K. P. et al. Resistive switching characteristics and mechanism of thermally grown WOx thin films. Journal of Applied Physics 110, 064505 (2011).
[63.] V. S. Fomenko, Handbook of thermionic properties, Electronic work functions and Richardson constants of Elements and Compounds, Ed. G. V. Samsonov, Springer US, 1966.
[64.] Hong, S. M. et al. Improved resistive switching properties by nitrogen doping in tungsten oxide thin films. Thin Solid Films 583, 81–85 (2015).
[65.] Pillai, P. B., Corpus Mendoza, A. N., De Souza, M. M., Bree, G. & Jeng, D. Extraction of Schottky barrier at the F-doped SnO2/ TiO_2 interface in Dye Sensitized solar cells. Journal of Renewable and Sustainable Energy 6, 013142 (2014).
[66.] Jameel, D. A. et al. Electrical performance of conducting polymer (SPAN) grown on GaAs with different substrate orientations. Applied Surface Science 387, 228–236 (2016).
[67.] Aydoğan, Ş., Sağlam, M. & Türüt, A. On the barrier inhomogeneities of polyaniline/p-Si/Al structure at low temperature. Applied Surface Science 250, 43–49 (2005).
[68.] Sun, B. et al. Non–zero-crossing current-voltage hysteresis behavior in memristive system. Materials Today Advances 6, 100056 (2020).
[69.] Qingjiang, L. et al. Memory Impedance in TiO_2 based Metal-Insulator-Metal Devices. Sci Rep 4, (2014).
[70.] Messerschmitt, F., Kubicek, M. & Rupp, J. L. M. How Does Moisture Affect the Physical Property of Memristance for Anionic-Electronic Resistive Switching Memories? Adv. Funct. Mater. 25, 5117–5125 (2015)
[71.] Muthuswamy, B. et al. Memristor modelling. in 2014 IEEE International Symposium on Circuits and Systems (ISCAS) (IEEE, 2014). doi:10.1109/iscas.2014.6865179.
[72.] Sun, B. et al. A Unified Capacitive-Coupled Memristive Model for the Nonpinched Current–Voltage Hysteresis Loop. Nano Lett. 19, 6461–6465 (2019).
[73.] Sung Lee, J., Buhm Lee, S., Kahng, B. & Won Noh, T. Two opposite hysteresis curves in semiconductors with mobile dopants. Appl. Phys. Lett. 102, 253503 (2013).
[74.] Jeong, D. S., Schroeder, H. & Waser, R. Mechanism for bipolar switching in aPt/ TiO_2 /Ptresistive switching cell. Phys. Rev. B 79, (2009).
[75.] Menzel, S. et al. Origin of the Ultra-nonlinear Switching Kinetics in Oxide-Based Resistive Switches. Adv. Funct. Mater. 21, 4487–4492 (2011).
[76.] Strukov, D. B. & Williams, R. S. Exponential ionic drift: fast switching and low volatility of thin-film memristors. Appl. Phys. A 94, 515–519 (2008).
[77.] C. Y. Chao et al., A Point Defect Model for Anodic Passive Films: I . Film Growth Kinetics. J. Electrochem. Soc. 128 1187 (1987)
[78.] Gablech, I. et al. Preparation of (001) preferentially oriented titanium thin films by ion-beam sputtering deposition on thermal silicon dioxide. J Mater Sci 51, 3329–3336 (2015).
[79.] Chang, Y.-H., Lin, H.-W. & Chen, C. Growth Mechanism of Self-Assembled TiO_2 Nanorod Arrays on Si Substrates Fabricated by Ti Anodization. J. Electrochem. Soc. 159, D512–D517 (2012).

[80.] Kao, K.-C. Dielectric phenomena in solids: with emphasis on physical concepts of electronic processes. (Academic Press, 2004).
[81.] Michalas, L., Khiat, A., Stathopoulos, S. & Prodromakis, T. Electrical characteristics of interfacial barriers at metal— TiO_2 contacts. J. Phys. D: Appl. Phys. 51, 425101 (2018).
[82.] Tao, M., Udeshi, D., Agarwal, S., Maldonado, E. & Kirk, W. P. Negative Schottky barrier between titanium and n-type Si() for low-resistance ohmic contacts. Solid-State Electronics 48, 335–338 (2004).

AUTHORS PUBLICATIONS AND OTHER INPUTS

PUBLICATIONS:

Influence of nitrogen species on the porous-alumina-assisted growth of TiO_2 nanocolumn arrays, Bendova, M., Kolar, J., Marik, M., Lednicky, T., Mozalev, A., Electrochimica Acta, 2018, 281, pp. 796–809

Resistive switching in TiO_2 nanocolumn arrays electrochemically grown, Marik, M., Mozalev, A., Hubalek, J., Bendova, M., Journal of Physics: Conference Series, 2017, 829(1), 012001

High-Performance Ammonia Gas Sensors Based on Plasma Treated Carbon Nanostructures Bannov, A.G., Jašek, O., Manakhov, A., …, Marik, M., Nečas, D., Zajíčková, L., IEEE Sensors Journal, 2017, 17(7), pp. 1964–1970, 7828047

Gold/polypyrrole nanorods for gas sensing application, Šetka, M., Drbohlavová, J., Vallejos, S., ...Marik, M., Llobet, E., Hubálek, J., Proceedings of SPIE - The International Society for Optical Engineering, 2017, 10246, 102461A

Electrochemical determination of adenine using a glassy carbon electrode modified with graphene oxide and polyaniline, Sharma, V., Hynek, D., Trnkova, L., ...Marik, M., Kizek, R., Hubalek, J., Microchimica Acta, 2016, 183(4), pp. 1299–1306

CONFERENCES

Applied nanostechnology and nanoscience International Conference - ANNIC 2016, Barcelona – oral presentation

Nanotech France 2016, Paris – oral presentation

ADDITIONAL EDUCATION

Seminar Smart Sensor Systems, Technical University of Delft, Netherland, 2014

University of Trento, CIBIO – research internship, autumn semester 2014

PROJECTS:

Czech Science Foundation (GA ČR) under the grant no. 15-23005Y – research team member

Advanced nanotechnologies and materials, start: 01.01.2014, end: 31.12.2016